



Available online at www.sciencedirect.com

ScienceDirect

Comput. Methods Appl. Mech. Engrg. 385 (2021) 114022

Computer methods in applied mechanics and engineering

www.elsevier.com/locate/cma

Modeling granular material dynamics and its two-way coupling with moving solid bodies using a continuum representation and the SPH method

Wei Hu^a, Milad Rakhsha^a, Lijing Yang^a, Ken Kamrin^b, Dan Negrut^{a,*}

^a Department of Mechanical Engineering, University of Wisconsin-Madison, Madison, WI 53706, USA ^b Department of Mechanical Engineering, Massachusetts Institute of Technology, Cambridge, MA 02139, USA

Received 3 December 2020; received in revised form 31 May 2021; accepted 25 June 2021 Available online xxxx

Abstract

We outline a continuum approach for treating discrete granular flows that holds across multiple scales: from experiments that focus on centimeter-size control volumes, to tests that involve landslides and large buildings. The time evolution of the continuum used to capture the granular dynamics is resolved in space via the smoothed particle hydrodynamics (SPH) method. The interaction between the granular material and immersed rigid bodies is posed and solved as a "fluid"—solid interaction (FSI) problem using boundary conditions enforcing (BCE) SPH particles rigidly attached onto the boundary of the body interacting with the granular material. A new penetration-based particle shifting technique (PPST) is proposed to enforce the particle regularity and thus a stable simulation. Several numerical experiments (angle of repose, ball drop, and cone penetration) are carried out to validate the accuracy of the proposed methodology. The approach is subsequently demonstrated in conjunction with a 3D landslide simulation and a plowing operation. The approach discussed has been implemented and can be used in an open source simulation platform publicly available on GitHub. The implementation leverages GPU computing. © 2021 Elsevier B.V. All rights reserved.

Keywords: Granular material; Continuum representation; Smoothed particle hydrodynamics; Fluid-solid interaction; Two-way coupling; Elasto-plasticity

1. Introduction

The interaction of granular material with moving solid bodies is encountered in many engineering applications, e.g. terramechanics, farming, astrophysics, pharma, etc., see, for instance, [1–8]. Depending on the size of the grain, in one cubic meter of sand there are in the neighborhood of two billion grains; when handling powders, a similar number of elements is contained in less than 10 cubic centimeters of powder. Fully resolved, discrete element method (DEM) simulations [9] on this scale, while not outright impossible [10], are impractical in a design engineering process owing to prohibitively long simulation times. Indeed, when it comes to early iterations through multiple concept designs, one needs accurate simulations that run in a reasonable amount of time on affordable hardware. This poses stiff challenges that should be met by combining advanced modeling and numerical solution techniques

E-mail address: negrut@wisc.edu (D. Negrut).

^{*} Corresponding author.

for granular material flows, rigid body dynamics, and their two-way coupling. A large body of work has been carried out to address these challenges. In the process, several numerical approaches have been proposed over time, which draw on the DEM [9,11–14], finite element method (FEM) [15–18], material point method (MPM) [19–22], and smoothed particle hydrodynamics (SPH) [23–25] method.

DEM is considered to be one of the most accurate methods in numerical simulation of granular material flows. However, DEM solves the dynamic equations of motion for each grain, individually. Hence, a fully resolved simulation of a practical granular material flow problem in conjunction with DEM will typically lead to very large degrees of freedom (DOF) counts, which poses both computational and storage challenges. Furthermore, the non-homogeneity of the grains in real-world problems poses another difficulty in the contact model and the contact-detection stage of the DEM, see, for instance, [26].

Continuum models of granular material flow have gained popularity over the last two decades as they have proved capable to address scale limitations in the DEM approach. They express the macro-scale behavior of the material by relating the stress to the strain and strain-rate fields, leading to smaller DOF counts compared to the DEM model. Many choices of space-discretization have been studied for solving the underlying equations of these continuum models. For instance, mesh-based numerical methods such as FEM have been investigated in [15,16]. They can accurately capture the general behavior of granular material flows but at a relatively high computational cost owing to the modeling of large mesh deformation. Indeed, the FEM elements tend to become ill-shaped when the granular material experiences large and nonuniform deformation, translation, or rotation. Re-meshing can be employed to fix this issue, yet this incurs additional computational costs and requires special care to preserve conservation laws [21].

The disadvantages of the mesh-based continuum approach mentioned above can be avoided by using particle-based or hybrid methods, such as SPH or MPM, respectively [27]. These two classes of Lagrangian methods proved effective in the simulation of granular material flows with large and nonuniform strains. For instance, hybrid methods such as MPM enjoy the advantages of both grid-based and mesh-free methods [28]. The idea behind MPM is to discretize the problem domain with both Lagrangian particles, referred to as "material points", and background "helper" grids as typically done in computational fluid dynamics. The equations of motion are solved on the background grid, while the state information is stored with the advecting material points. Despite the presence of the background grid, MPM does not encounter the drawbacks of mesh-based methods since the grid is fixed in space and does not deform. A modest computational cost is associated with an interpolation process that will repeatedly project particle-carried state information onto the underlying grid for expressing the balance equations (mass, momentum, energy) [29,30].

Unlike MPM, SPH is a meshless and grid-free Lagrangian particle method [31,32]. It can be used to solve partial differential equations (PDEs) associated with the mass, momentum, and energy conservation laws [33]. These PDEs are spatially discretized by employing a set of particles that possess material properties and interact with each other through kernel functions with compact support. The particles move according to inter-particle interactions and external forces. Due to its mesh-free and grid-free nature, the SPH method enables efficient modeling of granular flows with large strains and displacements. In [34], the SPH method was first utilized to model large deformation granular material flows with the Drucker-Prager model describing the elasto-plastic behavior of the material. The numerical results showed good agreement with experimental data. Similar strategies based on the Drucker-Prager model were employed in [24,35,36]. More recently, the interaction between granular material flows and rigid/flexible bodies was studied in [37-39]. However, these contributions only focused on the granular material flow and its interaction with fixed solid bodies. To the best of our knowledge, no physically validated approach has been reported that used the SPH method in a 3D context, while concentrating on the two-way coupling between the granular material and the dynamics of fully or partially immersed large implements in arbitrary 3D motion. Against this backdrop, we propose and validate a two-way coupling algorithm that captures both large deformation and strain of the granular material flows as well as large overall 3D motion of the solid bodies. To that end, we model the granular flow as an SPH-resolved continuum problem. The interaction between the granular material and immersed rigid bodies is posed and solved as an FSI problem using so-called boundary conditions enforcing (BCE) SPH particles [40,41], which are attached to the boundary of the implements. In previous work, this coupling algorithm was successfully applied to capture the interaction of fluids and rigid/flexible multi-body systems [41–44]. To represent the dynamics of dense granular material and update the stress field, we employ the rheology proposed in [21].

In Lagrangian particle-based methods, particle regularity is critical to ensuring numerical stability and accuracy [45–47]. However, highly nonuniform particle distributions may easily appear in SPH simulations when

particles advect with the flow. This aspect was addressed by the particle shifting technique (PST) proposed in [45]. Since the original approach did not handle problems with free surface, several attempts have been made to address this limitation [48,49]. They revolved around the idea of tracking the particles close to the free surface but the procedure was cumbersome, particularly so for three-dimensional problems. A second contribution made herein pertains to a new penetration-based particle shifting technique (PPST) that enforces a uniform distribution by slightly shifting particles away from streamlines without sacrificing efficiency or the Lagrangian nature of the approach. PPST is simple and can be readily implemented in three-dimensional free surface problems.

This contribution is organized as follows. Section 2 provides a detailed account of the proposed two-way coupling method for simulating granular material flows and their interaction with immersed solid bodies based on the SPH method. To that end, several topics are touched upon: consistent SPH discretization, rigid body dynamics, particle-shifting technique, enforcement of boundary condition, time integration, and a material stress update criterion. In Section 3, we demonstrate the accuracy and efficiency of the proposed method through numerical experiments. We model five different granular material flows — the angle of repose, ball drop, cone penetration, landslide interacting with surrounding obstacle, and plowing with an L-shaped plow. The numerical results obtained for the first three tests are compared with experimental data and numerical solutions obtained with the DEM method. We close with concluding remarks and directions for future work in Section 4.

2. Numerical method

2.1. Governing equations

Given the interest of this work in continuum modeling of granular material flows, in what follows the granular material will be regraded as a continuum "fluid"; the granular material flow with immersed solid bodies will be described as a "fluid"-solid interaction (FSI) system. Thus, the computational domain of an FSI system can be represented as $\Omega = \Omega_f \cup \Omega_s$, where Ω_f and Ω_s are the sub-domains occupied by the "fluid" and solid, respectively. The boundary Γ separates Ω_f and Ω_s , i.e., $\Gamma = \Omega_f \cap \Omega_s$.

2.1.1. Dynamic equation of the "fluid"

For a granular material flow, the "fluid" velocity \mathbf{u} and stress tensor $\boldsymbol{\sigma}$ enter the continuity and momentum balance equations as

$$\begin{cases} \frac{d\rho}{dt} = -\rho \nabla \cdot \mathbf{u} \\ \frac{d\mathbf{u}}{dt} = \frac{\nabla \sigma}{\rho} + \mathbf{f}_b \end{cases} \quad \text{for} \quad \mathbf{x} \in \Omega_f,$$
 (1)

where ρ is the density of the "fluid", and \mathbf{f}_b denotes the external force per unit mass, e.g., the gravity. Here, the stress tensor can be expressed as:

$$\sigma = -p\mathbf{I} + \tau \tag{2}$$

where p is the isotropic pressure and τ is the deviatoric component of the stress tensor. The isotropic pressure is defined as the trace of the stress tensor, i.e., $p = -\frac{1}{3}\text{tr}(\sigma) = -\frac{1}{3}(\sigma_{xx} + \sigma_{yy} + \sigma_{zz})$. According to Hooke's law, a linear elastic relation between the Jaumann stress rate tensor and elastic strain tensors [21,50–52] can be used to obtain the stress rate tensor as

$$\frac{d\sigma}{dt} = \dot{\phi} \cdot \sigma - \sigma \cdot \dot{\phi} + \overset{\triangle}{\sigma} \,, \tag{3}$$

where the rotation rate tensor is defined as $\dot{\phi} = \frac{1}{2}(\nabla \mathbf{u} - \nabla \mathbf{u}^{\mathsf{T}})$, the Jaumann rate of the stress tensor is expressed as

$$\overset{\triangle}{\sigma} = 2G(\dot{\boldsymbol{\varepsilon}} - \frac{1}{3}\operatorname{tr}(\dot{\boldsymbol{\varepsilon}})\mathbf{I}) + \frac{1}{3}K\operatorname{tr}(\dot{\boldsymbol{\varepsilon}})\mathbf{I} , \qquad (4)$$

and the elastic strain rate tensor is defined as $\dot{\boldsymbol{\varepsilon}} = \frac{1}{2}(\nabla \mathbf{u} + \nabla \mathbf{u}^{\mathsf{T}})$ in the absence of plastic flow. Herein, K denotes the bulk modulus of the material and satisfies $K = \frac{2(1+\nu)}{3(1-2\nu)}G$, where G and ν are the shear modulus and Poisson's ratio, respectively. Once the granular material starts to flow, the elastic strain rate tensor is defined as

$$\dot{\boldsymbol{\varepsilon}} = \frac{1}{2} (\nabla \mathbf{u} + \nabla \mathbf{u}^{\mathsf{T}}) - \frac{1}{\sqrt{2}} \dot{\lambda} \frac{\boldsymbol{\tau}}{\bar{\tau}} ,$$

in which the second term comes from the contribution of the plastic flow of the granular material, and $\dot{\lambda}$ and $\bar{\tau}$ are the plastic strain rate and equivalent shear stress, respectively, which will be defined in Section 2.6.

2.1.2. Dynamic equation of the solid bodies

We follow the formulation described in [53] to define the configuration of the system of bodies by a set of generalized coordinates for the position and orientation of a rigid body in the 3D Euclidean space as $\mathbf{r}_A \in \mathbb{R}^3$ and $\epsilon_A \in \mathbb{R}^4$; i.e., the absolute position of the center of mass, and the Euler parameters associated with orientation of body A. The Euler parameters satisfy the normalization constraint $\epsilon_A^{\mathsf{T}} \cdot \epsilon_A = 1$. Combining the set of generalized coordinates of different bodies for a system of n_b bodies, one can write the set of generalized coordinates describing the system at position level as $\mathbf{q} = \begin{bmatrix} \mathbf{r}_1^\mathsf{T}, \boldsymbol{\epsilon}_1^\mathsf{T}, \dots, \mathbf{r}_{n_b}^\mathsf{T}, \boldsymbol{\epsilon}_{n_b}^\mathsf{T} \end{bmatrix}^\mathsf{T} \in \mathbb{R}^{7n_b}$, and at velocity level as $\dot{\mathbf{q}} = \begin{bmatrix} \dot{\mathbf{r}}_1^\mathsf{T}, \dot{\boldsymbol{\epsilon}}_1^\mathsf{T}, \dots, \dot{\mathbf{r}}_{n_b}^\mathsf{T}, \dot{\boldsymbol{\epsilon}}_{n_b}^\mathsf{T} \end{bmatrix}^\mathsf{T} \in \mathbb{R}^{7n_b}$. Instead of using the time derivative of the Euler parameters, one may choose to use angular velocities to describe the state of the system at the velocity level by $\mathbf{u} = \begin{bmatrix} \dot{\mathbf{r}}_1^\mathsf{T}, \bar{\boldsymbol{\omega}}_1^\mathsf{T}, \dots, \dot{\mathbf{r}}_{n_b}^\mathsf{T}, \bar{\boldsymbol{\omega}}_{n_b}^\mathsf{T} \end{bmatrix}^\mathsf{T} \in \mathbb{R}^{6n_b}$, which reduces the problem size. The transformation from the derivatives of Euler parameters, $\dot{\boldsymbol{\epsilon}}_A$, to angular velocities represented in the body-fixed frame, $\bar{\omega}_A$, for each body is governed by $\dot{\epsilon}_A = \frac{1}{2} \bar{\mathbf{Q}}^{\mathsf{T}}(\epsilon_A) \bar{\omega}_A$, where matrix $\mathbf{Q} \in \mathbb{R}^{3\times 4}$ depends linearly on the Euler parameters ϵ_A . Therefore, a block diagonal matrix $\mathbf{L}(\mathbf{q}) \equiv \operatorname{diag}\left[\mathbf{I}_{3\times3}, \frac{1}{2}\mathbf{Q}^{\mathsf{T}}(\epsilon_1), \dots, \mathbf{I}_{3\times3}, \frac{1}{2}\mathbf{Q}^{\mathsf{T}}(\epsilon_{nb})\right] \in$ $\mathbb{R}^{7n_b \times 6n_b}$ is used to express via $\dot{\mathbf{q}} = \mathbf{L}(\mathbf{q})\mathbf{u}$, the relationship between $\dot{\mathbf{q}}$ and \mathbf{u} , where $\mathbf{I}_{3\times3}$ is the identity matrix [53].

The constrained Newton-Euler equations of motion that describe the motion of a system of bodies interacting through friction, contact, and bilateral constraints, assume the following form of a differential variational inequality (DVI) problem, see, for instance, [54,55]:

$$\dot{\mathbf{q}} = \mathbf{L}(\mathbf{q})\mathbf{u} \tag{5a}$$

$$\mathbf{M}\dot{\mathbf{u}} = \mathbf{f}(t, \mathbf{q}, \mathbf{u}) + \sum_{k \in \mathcal{A}(\mathbf{q}, \delta)} \left(\gamma_{k,n} \, \mathbf{D}_{k,n} + \gamma_{k,v} \, \mathbf{D}_{k,v} + \gamma_{k,w} \, \mathbf{D}_{k,w} \right)$$

$$k \in \mathcal{A}(\mathbf{q}, \delta) : 0 \le \gamma_{k,n} \perp \Phi_{k}(\mathbf{q}) \ge 0$$

$$(5c)$$

$$k \in \mathcal{A}(\mathbf{q}, \delta) : 0 \le \gamma_{k,n} \perp \Phi_k(\mathbf{q}) \ge 0$$
 (5c)

$$(\gamma_{k,v}, \gamma_{k,w}) = \underset{\sqrt{(\gamma_{k,v})^2 + (\gamma_{k,w})^2} \le \mu_k^f \gamma_{k,n}}{\operatorname{argmin}} \mathbf{u}^{\mathsf{T}} (\gamma_{k,v} \mathbf{D}_{k,v} + \gamma_{k,w} \mathbf{D}_{k,w}) ,$$

$$(5d)$$

where $\mathbf{f}(t, \mathbf{q}, \mathbf{u})$ are the external forces; **M** is the constant system mass matrix; and, $\mathcal{A}(\mathbf{q}, \delta)$ is the set of active and potential unilateral constraints based on the bodies that are mutually less than a gap δ apart. For contact k, the tangent space generator $\mathbf{D}_k \equiv [\mathbf{D}_{k,n}, \mathbf{D}_{k,v}, \mathbf{D}_{k,w}] \in \mathbb{R}^{6n_b \times 3}$ is defined as [55]

$$\boldsymbol{D}_{k} = \begin{bmatrix} \boldsymbol{0}_{3\times3}, \dots, -\boldsymbol{A}_{k}^{\intercal}, \boldsymbol{A}_{k}^{\intercal}\boldsymbol{A}_{A}\tilde{\tilde{\boldsymbol{s}}}_{k,A}, \boldsymbol{0}_{3\times3}, \dots, \boldsymbol{0}_{3\times3}, \boldsymbol{A}_{k}^{\intercal}, -\boldsymbol{A}_{k}^{\intercal}\boldsymbol{A}_{B}\tilde{\tilde{\boldsymbol{s}}}_{k,B}, \dots, \boldsymbol{0}_{3\times3} \end{bmatrix}^{\intercal},$$

where $\mathbf{A}_k = [\mathbf{n}_k, \mathbf{v}_k, \mathbf{w}_k] \in \mathbb{R}^{3 \times 3}$ is the orientation matrix associated with contact k; $\mathbf{A}_A = \mathbf{A}(\epsilon_A)$ and $\mathbf{A}_B = \mathbf{A}(\epsilon_B)$ are the rotation matrices; ϵ_A and $\epsilon_B \in \mathbb{R}^4$ are the Euler parameters associated with orientation of body A and B respectively; and the vectors $\bar{\mathbf{s}}_{k,A}$ and $\bar{\mathbf{s}}_{k,B} \in \mathbb{R}^3$ represent the contact point positions in body-relative coordinates as shown in Fig. 1. Above, the operator "tilde" applied to a three dimensional vector **a** produces a matrix $\tilde{\mathbf{a}} \in \mathbb{R}^{3 \times 3}$ such that $\mathbf{a} \times \mathbf{b} = \tilde{\mathbf{a}} \mathbf{b}$ for all $\mathbf{b} \in \mathbb{R}^3$.

Eq. (5c) captures a complementarity condition between Φ , the gap (distance) between bodies A and B at the contact point, and $\gamma_{k,n}$, the Lagrange multiplier for the normal/contact force associated with the contact k. The complementarity condition states that of $\gamma_{k,n}$ and Φ , at least one is zero and the other one is nonnegative. Indeed, when the gap function is zero (contact is present), the normal contact force is nonnegative; and, conversely, when the normal contact force is zero the gap function is nonnegative. The forces associated with contact k can be expressed as $f_{k,N} = \gamma_{k,n} n_k$, and $f_{k,T} = \gamma_{k,v} v_i + \gamma_{k,w} w_k$, which are the contact and friction forces, respectively; and, $\gamma_{k,w}$ and $\gamma_{k,v}$ are the components of the friction force in the tangent plane. Finally, $\gamma_{k,w}$ and $\gamma_{k,v}$ are the solution of an optimization problem that is posed in Eq. (5d) to maximize the dissipation energy, see [56]. The DVI problem stated in Eq. (5) can be solved with a variety of techniques, see [57–66].

2.2. Spatial discretization

In the SPH method, the partial differential equations associated with the balance laws of the continuum, i.e., mass and momentum equations, are spatially discretized using SPH particles that advect with the flow field. The particles

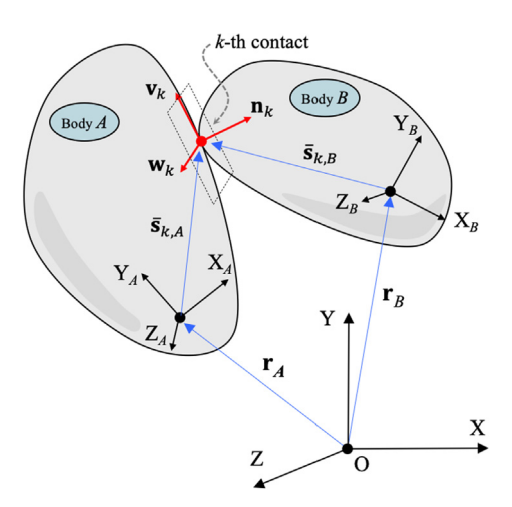


Fig. 1. Contact between two bodies.

within Ω_f and Ω_s are referred to as "fluid" and BCE particles, respectively. The motion of the BCE particles is described by the motion of the solid bodies to which they are rigidly attached. The value of a function f at the location of particle i is then approximated as [33]

$$f_i = \sum_j f_j W_{ij} \mathcal{V}_j , \qquad (6)$$

where a "volume" associated with an SPH particle is defined as $V_i = (\sum_j W_{ij})^{-1}$. Hence, the mass associated with an SPH particle is given by $m_i = \rho_i V_i$. In Eq. (6), $W_{ij} = W(\mathbf{r}_{ij})$ is the kernel function, which in this work is assumed to be a cubic spline

$$W_{ij} = \alpha_d \begin{cases} \frac{2}{3} - R^2 + \frac{1}{2}R^3 & 0 \le R < 1\\ \frac{1}{6}(2 - R)^3 & 1 \le R < 2\\ 0 & R \ge 2, \end{cases}$$
 (7)

where the constant α_d assumes the value of $15/(7\pi h^2)$ for two-dimensional (2D) simulations and $3/(2\pi h^3)$ for three-dimensional (3D) simulations; $R = \frac{r_{ij}}{h}$ with h denoting the kernel length and $r_{ij} = \|\mathbf{r}_{ij}\|$. Here, $\mathbf{r}_{ij} = \mathbf{x}_i - \mathbf{x}_j$ where \mathbf{x}_i is the position of particle i. For future reference, $\mathbf{e}_{ij} = \mathbf{r}_{ij}/r_{ij}$. With this kernel function, a field value at the location of a SPH particle j contributes to the summation in Eq. (6) for approximating the function at location i only when $j \in \mathcal{N}_{h,i} = \{\mathbf{x}_j : r_{ij} < 2h\}$. The neighbor list of particle i is in a support domain with a constant size and should be updated at each time step during the simulation since most of the SPH particles would advect along with the granular flow. However, in some specific areas of the simulation domain, the neighbor list can be unchanged throughout the simulation. Thus the Lagrangian kernel proposed in [67,68] can be more efficient than the Eulerian kernel used in this work. In the Lagrangian kernel, the neighbor list is only calculated once at the beginning of the simulation, which leads to an efficiency improvement. Considering that for the applications of interest most the SPH particles are "flowing", the implementation herein used an Eulerian kernel that requires a neighbor list update at each time step.

In the consistent SPH discretization [46,47,69–71], the gradient of the function f at the location of SPH particle i is approximated as

$$\nabla f_i = \sum_j (f_j - f_i) \left(\mathbf{G}_i \cdot \nabla_i W_{ij} \right) \mathcal{V}_j ,$$

where the partial differentiation of the kernel function with respect to \mathbf{x}_i is

$$\nabla_i W_{ij} = \alpha_d \frac{1}{h} \frac{\mathbf{r}_{ij}}{r_{ij}} \begin{cases} -2R + \frac{3}{2}R^2 & 0 \le R < 1 \\ -\frac{1}{2}(2-R)^2 & 1 \le R < 2 \\ 0 & R \ge 2. \end{cases}$$

The inverse of the correction matrix G_i in 3D space can be expressed as:

$$\mathbf{G}_{i}^{-1} = -\sum_{j} \mathbf{r}_{ij} \nabla_{i} W_{ij} \mathcal{V}_{j} = -\begin{bmatrix} \sum_{j} r_{ij}^{x} \nabla_{i,x} W_{ij} \mathcal{V}_{j} & \sum_{j} r_{ij}^{x} \nabla_{i,y} W_{ij} \mathcal{V}_{j} & \sum_{j} r_{ij}^{x} \nabla_{i,z} W_{ij} \mathcal{V}_{j} \\ \sum_{j} r_{ij}^{y} \nabla_{i,x} W_{ij} \mathcal{V}_{j} & \sum_{j} r_{ij}^{y} \nabla_{i,y} W_{ij} \mathcal{V}_{j} & \sum_{j} r_{ij}^{y} \nabla_{i,z} W_{ij} \mathcal{V}_{j} \\ \sum_{j} r_{ij}^{z} \nabla_{i,x} W_{ij} \mathcal{V}_{j} & \sum_{j} r_{ij}^{z} \nabla_{i,y} W_{ij} \mathcal{V}_{j} & \sum_{j} r_{ij}^{z} \nabla_{i,z} W_{ij} \mathcal{V}_{j} \end{bmatrix}.$$

Previous studies have demonstrated that this discretization of the gradient, which involves the symmetric correction matrices $\mathbf{G}_i \in \mathbb{R}^{3\times 3}$, guarantees the exact gradient for linear functions regardless of the ratio of $h/\Delta x$ and hence displays consistency [69]. Herein, Δx is the particle spacing. A detailed description of \mathbf{G}_i can be found in [70]. Hence, the consistent SPH discretization of the governing equations is given as:

$$\frac{d\rho_i}{dt} = -\rho_i \sum_i (\mathbf{u}_j - \mathbf{u}_i) \cdot \left(\mathbf{G}_i \cdot \nabla_i W_{ij} \right) \mathcal{V}_j , \qquad (8)$$

$$\frac{d\mathbf{u}_i}{dt} = \frac{1}{\rho_i} \sum_{i}^{J} (\boldsymbol{\sigma}_j - \boldsymbol{\sigma}_i) \cdot \left(\mathbf{G}_i \cdot \nabla_i W_{ij} \right) \mathcal{V}_j + \mathbf{f}_{b,i}. \tag{9}$$

The consistent SPH discretization of the strain rate tensor and rotation rate tensor are given by:

$$\dot{\boldsymbol{\varepsilon}}_i = \frac{1}{2} \sum_i (\mathbf{u}_{ji} + \mathbf{u}_{ji}^{\mathsf{T}}) \left(\mathbf{G}_i \cdot \nabla_i W_{ij} \right) \mathcal{V}_j , \qquad (10)$$

$$\dot{\boldsymbol{\phi}}_{i} = \frac{1}{2} \sum_{i}^{J} (\mathbf{u}_{ji} - \mathbf{u}_{ji}^{\mathsf{T}}) \left(\mathbf{G}_{i} \cdot \nabla_{i} W_{ij} \right) \mathcal{V}_{j}. \tag{11}$$

Substituting Eqs. (10) and (11) into Eq. (3) yields a consistent SPH discretization of the stress rate tensor as:

$$\frac{d\boldsymbol{\sigma}_{i}}{dt} = \frac{1}{2} \left\{ \left[\sum_{j} (\mathbf{u}_{ji} - \mathbf{u}_{ji}^{\mathsf{T}}) \left(\mathbf{G}_{i} \cdot \nabla_{i} W_{ij} \right) \mathcal{V}_{j} \right] \boldsymbol{\sigma}_{i} - \boldsymbol{\sigma}_{i} \left[\sum_{j} (\mathbf{u}_{ji} - \mathbf{u}_{ji}^{\mathsf{T}}) \left(\mathbf{G}_{i} \cdot \nabla_{i} W_{ij} \right) \mathcal{V}_{j} \right] \right\}
+ G \left\{ \left[\sum_{j} (\mathbf{u}_{ji} + \mathbf{u}_{ji}^{\mathsf{T}}) \left(\mathbf{G}_{i} \cdot \nabla_{i} W_{ij} \right) \mathcal{V}_{j} \right] - \frac{1}{3} \text{tr} \left(\sum_{j} (\mathbf{u}_{ji} + \mathbf{u}_{ji}^{\mathsf{T}}) \left(\mathbf{G}_{i} \cdot \nabla_{i} W_{ij} \right) \mathcal{V}_{j} \right) \mathbf{I} \right\}
+ \frac{1}{6} K \left\{ \text{tr} \left(\sum_{j} (\mathbf{u}_{ji} + \mathbf{u}_{ji}^{\mathsf{T}}) \left(\mathbf{G}_{i} \cdot \nabla_{i} W_{ij} \right) \mathcal{V}_{j} \right) \mathbf{I} \right\} ,$$
(12)

Finally, the location of the SPH particle i is related to its velocity as

$$\frac{d\mathbf{x}_i}{dt} = \mathbf{u}_i - \xi \sum_i \mathbf{u}_{ij} W_{ij} \mathcal{V}_j , \qquad (13)$$

where the correction term that includes the coefficient ξ enforces the condition that a particle advects at a velocity close to the average velocity of its neighboring particles. This is the so-called XSPH technique [72], which induces orderly particle advection and effectively reduces the penetration between SPH particles. The coefficient ξ is a constant between 0 and 1, which is set to 0.5 in this study. It is noted that through ξ , one can control energy dissipation in the simulation; this is similar, for instance, to the integration coefficients one can tune in the Newmark, HHT, or generalized- α methods in continuum mechanics [73–75]. To gauge its impact, we performed a series of simulations with different values of ξ in the angle of repose test in Section 3.1 and explained why 0.5 was the value of choice for ξ , which led to an approximately 0.2% error in the kinetic energy. As an alternative, a different and conservative scheme is discussed [76,77].

2.3. Boundary conditions

The discussion in this subsection draws on the schematic in Fig. 2. The "fluid"-solid, two-way coupling is modeled by simultaneously imposing a no-slip boundary condition (BC) for the "fluid" at the solid boundary; and,

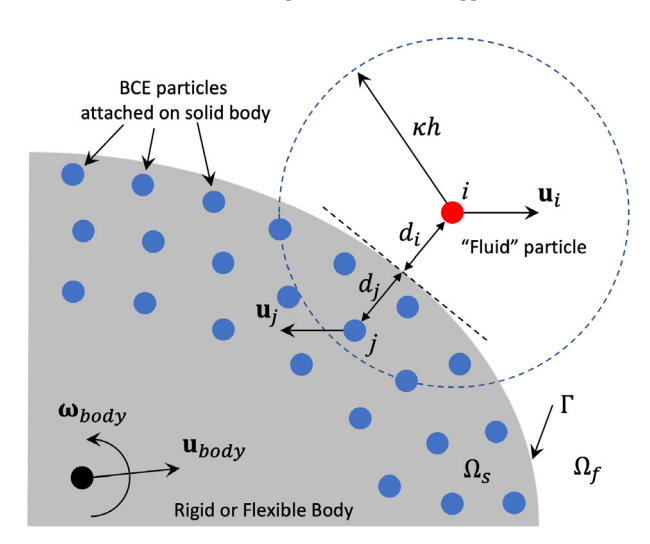


Fig. 2. "Fluid" particles (red) and BCE particles (blue) near the "fluid"-solid boundary. Velocities are extrapolated to the BCE particles to impose the Dirichlet boundary condition. (For interpretation of the references to color in this figure legend, the reader is referred to the web version of this article.)

for the solid body, by accounting for the force and torque exerted by the "fluid". The no-slip BC assumes the generic form $\mathbf{u}(\mathbf{x}) = \mathbf{u}_B(\mathbf{x})$; i.e., at any point of the boundary $\mathbf{x} \in \Gamma$, the velocity \mathbf{u} of the "fluid" and \mathbf{u}_B of the solid are identical. Note that this condition should hold regardless whether the solid is rigid or flexible. For a rigid body, the velocity at the boundary can be expeditiously expressed as:

$$\mathbf{u}_B = \mathbf{u}_{body} + \boldsymbol{\omega}_{body} \times \mathbf{r}_c(\mathbf{x}) \qquad \text{for } \mathbf{x} \in \Gamma, \tag{14}$$

where \mathbf{u}_{body} and $\boldsymbol{\omega}_{body}$ denote the linear and angular velocities of the rigid body, respectively, and $\mathbf{r}_c(\mathbf{x})$ denotes the vector from the center-of-mass of the rigid body to the location $\mathbf{x} \in \Gamma$. Although the methodology presented here applies equally well to rigid and flexible bodies, the presentation continues with an assumption that the solid body is rigid (infinitely stiff). For flexible bodies the expression of the BCE particle velocity is more involved as it requires the time derivative of the shape functions.

To accurately impose the no-slip boundary condition for the "fluid" velocity, the SPH approximations of velocity and its spatial derivatives for the SPH "fluid" particles near the "fluid"-solid boundary must attain full support of the kernel contained in the domain ($\Omega_f \cup \Omega_s$). We follow the approach proposed in literature [47,70,78–80] to lay several layers of BCE particles in the solid domain near the boundary, as illustrated in Fig. 2. These BCE particles are assigned velocities linearly extrapolated from the velocities of "fluid" particles, i.e.,

$$\mathbf{u}_j = \frac{d_j}{d_i}(\mathbf{u}_B - \mathbf{u}_i) + \mathbf{u}_B , \qquad (15)$$

where i is a "fluid" particle; j represents a BCE particle; d_i and d_j denote the closest perpendicular distances to the boundary for the "fluid" and BCE particles, respectively; and \mathbf{u}_B is the velocity of the solid boundary as in Eq. (14). It is noted that the extrapolated velocity here is only used to enforce the no-slip boundary condition, and will not be used to displace the BCE particles; the BCE particles will move as the solid body moves. For problems with simple geometry, d_i and d_j distances can be easily obtained whereas for more complex geometry, d_i and d_j in Eq. (15) are approximated by [80]

$$d_i = \kappa h_i(2\chi_i - 1), \qquad d_j = \kappa h_j(2\chi_j - 1),$$

where the length of the kernel for particle i is h_i , and $\kappa = 2$ for the cubic spline function used herein. The indicator χ used to differentiate "fluid" i and solid j particles is given as

$$\chi_i = \frac{\sum_{k \in \Omega_f} W_{ik}}{\sum_{k \in \Omega_f \cup \Omega_s} W_{ik}} \quad , \qquad \qquad \chi_j = \frac{\sum_{k \in \Omega_s} W_{jk}}{\sum_{k \in \Omega_f \cup \Omega_s} W_{jk}} \; .$$

The stress tensor at the location of a BCE particle j is calculated as [25]

$$\sigma_j = \frac{\sum_{k \in \Omega_f} \sigma_k W_{jk} + [diag(\mathbf{f}_b - \mathbf{f}_j)] \sum_{k \in \Omega_f} \rho_k [diag(\mathbf{r}_{jk})] W_{jk}}{\sum_{k \in \Omega_f} W_{jk}} \; ,$$

where the function $diag(\mathbf{x})$ creates a diagonal matrix from a vector \mathbf{x} ; \mathbf{r}_{jc} denotes the vector from the center-of-mass of the solid body pointing to the BCE particle j attached on this solid body; \mathbf{f}_b is the body force for the "fluid" (e.g., the gravity force); and \mathbf{f}_j is the inertial force associated with the BCE particle and evaluated as

$$\mathbf{f}_{i} = \dot{\mathbf{u}}_{body} + \dot{\boldsymbol{\omega}}_{body} \times \mathbf{r}_{ic} + \boldsymbol{\omega}_{body} \times (\boldsymbol{\omega}_{body} \times \mathbf{r}_{ic}) .$$

The total force \mathbf{F}_{body} and torque \mathbf{T}_{body} exerted by the "fluid" on the solid is computed by summing the forces contributed by the "fluid" particles onto BCE particles as in the conservative SPH methods [81]. The total force and torque applied on the immersed solid is obtained by summing the forces at the location of each BCE particle, $m_i \dot{\mathbf{u}}_i$, from Eq. (9) as

$$\mathbf{F}_{body} = \sum_{j \in \Omega_s} m_j \, \dot{\mathbf{u}}_j \quad \text{and} \quad \mathbf{T}_{body} = \sum_{j \in \Omega_s} \mathbf{r}_{jc} \times (m_j \, \dot{\mathbf{u}}_j) \; .$$

2.4. Enforcing particle regularity via PPST

The advection of the SPH particles can lead to scenarios characterized by high particle disorder and/or regions with high particle depletion/plenitude. We provision against such scenarios, which can undermine the accuracy and stability attributes of the numerical solution, by employing a new approach in which the SPH particles are slightly shifting away from streamlines to enforce a uniform particle distribution. The particle shifting technique (PST) in incompressible SPH was promoted in [45] and subsequently found to be effective in sustaining particle regularity and numerical stability in [45–47]. This shifting technique was also applied in a weakly compressible SPH formulation [82]. However, the original particle shifting scheme [45] requires a complete support domain for each particle, which precludes its use for problems with free surfaces. For such problems, particle deficiency near free surface lead to a continuous shifting artifact in the normal direction to free surface, expanding the problem domain. To overcome this deficiency, efforts have been made to track the free surface particles and treat them differently, e.g. by removing the normal component of the shifting vector for free surface particles [48,49]. However, for general three-dimensional problems, tracking the free surface particle is usually a challenging task.

We propose a penetration-based particle shifting technique (PPST) that requires no tracking for free surface particles, is stable, and simple to implement for general three-dimensional free surface problems. The technique attaches at the location of each SPH particle a fictitious sphere of diameter $D_{s,i} = 2\sqrt[3]{\frac{3m_i}{4\pi\rho_i}}$, where m_i is the mass of particle i, and computes the particle shifting vector as

$$\delta \mathbf{r}_{i} = \begin{cases} \beta_{1} \| \mathbf{u}_{i} \| \Delta t \sum_{j} \delta r_{ij} \mathbf{e}_{ij} & \delta r_{ij} > 0 \\ \beta_{2} \| \mathbf{u}_{i} \| \Delta t \sum_{j} \delta r_{ij} \mathbf{e}_{ij} & \delta r_{0} < \delta r_{ij} \leq 0 \\ \beta_{2} \| \mathbf{u}_{i} \| \Delta t \sum_{j} \delta r_{0} \mathbf{e}_{ij} & \delta r_{ij} \leq \delta r_{0}, \end{cases}$$

$$(16)$$

where the penetration between particle i and j is defined as $\delta r_{ij} = \frac{D_{s,i} - r_{ij}}{D_{s,i}}$, and Δt is the integration time step. Based on this definition, the penetration can be positive when $r_{ij} < D_{s,i}$, or negative when $r_{ij} > D_{s,i}$. It was reported in [45] that the shifting vector should be large enough to prevent disordered particle distribution and small enough not to cause inaccuracy and instability. In this work, the adjustable dimensionless parameters β_1 and β_2 are set as $\beta_1 = 3$ and $\beta_2 = 1$, which will guarantee that the ratio of $\frac{\|\delta r_i\|}{\|\mathbf{u}_i\|\Delta t} \times 100\%$ is less than 5%. The critical value for the penetration, i.e. δr_0 , which controls the lower bound of the negative penetration between particles, is set to $\delta r_0 = -0.1$. With this, at the end of each time step, the position of particle i is shifted by $\mathbf{x}_i^{new} = \mathbf{x}_i + \delta \mathbf{r}_i$. Accordingly, the volume of each particle is calculated as $\mathcal{V}_i^{new} = (\sum_j W_{ij})^{-1}$, and the density is calculated as $\rho_i^{new} = \frac{m_i}{\mathcal{V}_i^{new}}$. The velocity \mathbf{u}_i is corrected to a new value at the shifted new position via a second-order interpolation:

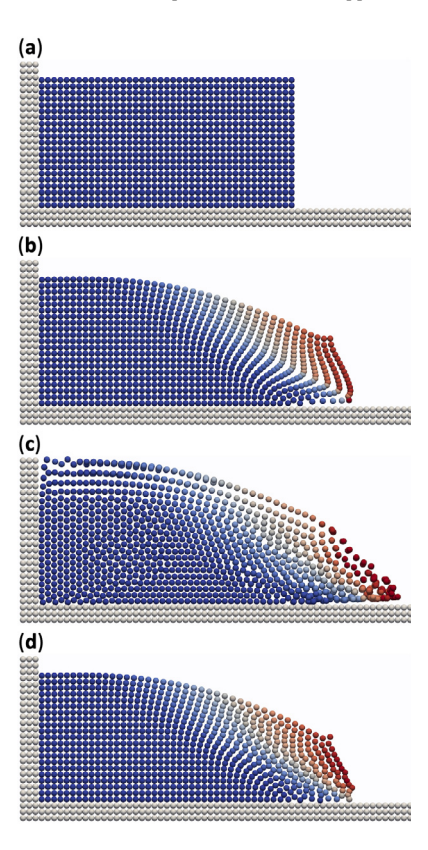


Fig. 3. (a) Initial particle distribution of the granular collapse (b) SPH particle distribution without particle shifting (c) SPH particle distribution with PST proposed in [45] (d) SPH particle distribution with PPST proposed in this paper.

 $\mathbf{u}_i \to \mathbf{u}_i^{new}$; interpolation details may be found in [70,71]. Fig. 3 demonstrates the improvement of the new proposed PPST via a granular collapse problem. In Fig. 3(d) there is neither the particle expansion observed in the original PST [45], nor the space voids that appear in simulation without PST. The key difference between the proposed PPST and the original PST pertains to the calculation of the shift vector for particle i in relation to the position of the other neighbor particles $j \in \mathcal{N}_{h,i}$. In the PPST scheme, if particle j is too close to particle i, the direction of the contribution vector is from j to i; otherwise, it will change from i to j. In the original PST scheme [45], the direction of the contribution of j is fixed to a direction from j to i, regardless of where particle j is. Thus, the inner particles will always be "pushing" the surface particles, which explains the particle expansion in Fig. 3(c). In the proposed PPST scheme, once a surface particle starts to expand, the inner particles will switch from "pushing" to "pulling" the surface particle, which explains the good particle distribution shown in Fig. 3(d).

2.5. Time integration

The field variables at the location of the "fluid" particles are updated via a standard second-order, explicit predictor–corrector scheme [72,83]. The intermediate velocity $\bar{\mathbf{u}}_i$, position $\bar{\mathbf{x}}_i$ and stress tensor $\bar{\boldsymbol{\sigma}}_i$ at the intermediate time step $t + \frac{\Delta t}{2}$ are first predicted as:

$$\begin{cases} \bar{\mathbf{u}}_i(t + \frac{\Delta t}{2}) = \mathbf{u}_i(t) + \frac{\Delta t}{2}\mathbf{a}_i(t) \\ \bar{\boldsymbol{\sigma}}_i(t + \frac{\Delta t}{2}) = \boldsymbol{\sigma}_i(t) + \frac{\Delta t}{2}\mathbf{b}_i(t) \\ \bar{\mathbf{x}}_i(t + \frac{\Delta t}{2}) = \mathbf{x}_i(t) + \frac{\Delta t}{2}\mathbf{c}_i(t). \end{cases}$$

The values $\mathbf{a}_i = \frac{d\mathbf{u}_i}{dt}$, $\mathbf{b}_i = \frac{d\mathbf{s}_i}{dt}$ and $\mathbf{c}_i = \frac{d\mathbf{x}_i}{dt}$ are determined from Eqs. (9), (12) and (13). The intermediate pressure $\bar{p}_i(t + \frac{\Delta t}{2})$ is then obtained via the trace of the stress tensor $\bar{\sigma}_i(t + \frac{\Delta t}{2})$. After the predictor step, $\mathbf{a}_i(t + \frac{\Delta t}{2})$, $\mathbf{b}_i(t + \frac{\Delta t}{2})$

and $\mathbf{c}_i(t+\frac{\Delta t}{2})$ are evaluated and subsequently used in the corrector step:

$$\begin{cases} \mathbf{u}_{i}(t + \frac{\Delta t}{2}) = \mathbf{u}_{i}(t) + \frac{\Delta t}{2}\mathbf{a}_{i}(t + \frac{\Delta t}{2}) \\ \mathbf{\sigma}_{i}(t + \frac{\Delta t}{2}) = \mathbf{\sigma}_{i}(t) + \frac{\Delta t}{2}\mathbf{b}_{i}(t + \frac{\Delta t}{2}) \\ \mathbf{x}_{i}(t + \frac{\Delta t}{2}) = \mathbf{x}_{i}(t) + \frac{\Delta t}{2}\mathbf{c}_{i}(t + \frac{\Delta t}{2}). \end{cases}$$

Finally, the particle's velocity and position at $t + \Delta t$ are updated by:

$$\begin{cases} \mathbf{u}_{i}(t + \Delta t) = 2\mathbf{u}_{i}(t + \frac{\Delta t}{2}) - \mathbf{u}_{i}(t) \\ \boldsymbol{\sigma}_{i}(t + \Delta t) = 2\boldsymbol{\sigma}_{i}(t + \frac{\Delta t}{2}) - \boldsymbol{\sigma}_{i}(t) \\ \mathbf{x}_{i}(t + \Delta t) = 2\mathbf{x}_{i}(t + \frac{\Delta t}{2}) - \mathbf{x}_{i}(t). \end{cases}$$

In this predictor–corrector scheme, the time step Δt is constrained by the CFL condition [84].

2.6. Post-processing strategy for the stress tensor

To represent the dynamics of the granular material, we employ a rheology proposed in conjunction with the material point method (MPM) [21]. The stress tensor can be first updated explicitly from t_n to t_{n+1} in terms of ρ^n , \mathbf{u}^n and σ^n according to the predictor–corrector scheme described in Section 2.5. Then the stress tensor can be corrected based on a post-processing strategy which is implemented in four steps:

STEP 1: Update the stress tensor to an intermediate value σ^* according to the predictor–corrector integration scheme, i.e.

$$\sigma^* = \sigma(t + \Delta t) \,, \tag{17}$$

and use Eq. (2) to compute τ^* and p^* . If $p^* < 0$, then simply set $\sigma^{n+1} = 0$ and advance the simulation time by one time step, i.e., start a new integration step all over again.

STEP 2 : Calculate $\bar{\tau}^*$ through the double inner product of the intermediate deviatoric component of the stress tensor as

$$\bar{\tau}^* = \sqrt{\frac{1}{2}}(\tau_{\alpha\beta}^*) : (\tau_{\alpha\beta}^*),\tag{18}$$

STEP 3: Calculate S_0 based on the static friction coefficient μ_s

$$S_0 = \mu_s p^*. \tag{19}$$

STEP 4: If $\bar{\tau}^* < S_0$, no plastic flow occurs; use τ^* as the deviatoric component of the stress tensor at the end of this time step

$$\boldsymbol{\tau}^{n+1} = \boldsymbol{\tau}^*, \quad p^{n+1} = p^*, \quad \boldsymbol{\sigma}^{n+1} = \boldsymbol{\sigma}^*.$$
(20)

Else, if $\bar{\tau}^* \geq S_0$, plastic flow occurs; the Drucker-Prager yield criterion is used to scale the deviatoric component of the stress tensor back to the yield surface

$$\boldsymbol{\tau}^{n+1} = \frac{\mu p^*}{\bar{\tau}^*} \boldsymbol{\tau}^* , \quad p^{n+1} = p^* , \quad \boldsymbol{\sigma}^{n+1} = -p^{n+1} \mathbf{I} + \boldsymbol{\tau}^{n+1}.$$
 (21)

Above, the friction coefficient is defined as $\mu = \mu_s + \frac{\mu_2 - \mu_s}{I_0/I + 1}$ [21]; I_0 is a material constant chosen between 0.03 and 0.05 in this work; $I = \dot{\lambda} d \sqrt{\frac{\rho_0}{p^{n+1}}}$ is the inertial number; μ_2 is the limiting value of μ when $I \to \infty$; d is the average diameter of the granular particles; and $\dot{\lambda} = \frac{\bar{\tau}^* - \bar{\tau}^n}{G\Delta t}$ is the plastic strain rate. To update the stress tensor, we first use Eq. (3) and the predictor-corrector integration scheme without considering the contribution from the plastic flow, and we will get the σ^* in STEP 1. By adopting the Drucker-Prager yield criterion and the four-step post-processing strategy above, the stress tensor can be corrected at the end of each integration step, i.e., we will get the final stress tensor σ^{n+1} . It is noted that the four-step strategy will automatically deal with the contribution from the plastic flow, thus no need to consider the plasticity during the integration stage which is described in Section 2.5.

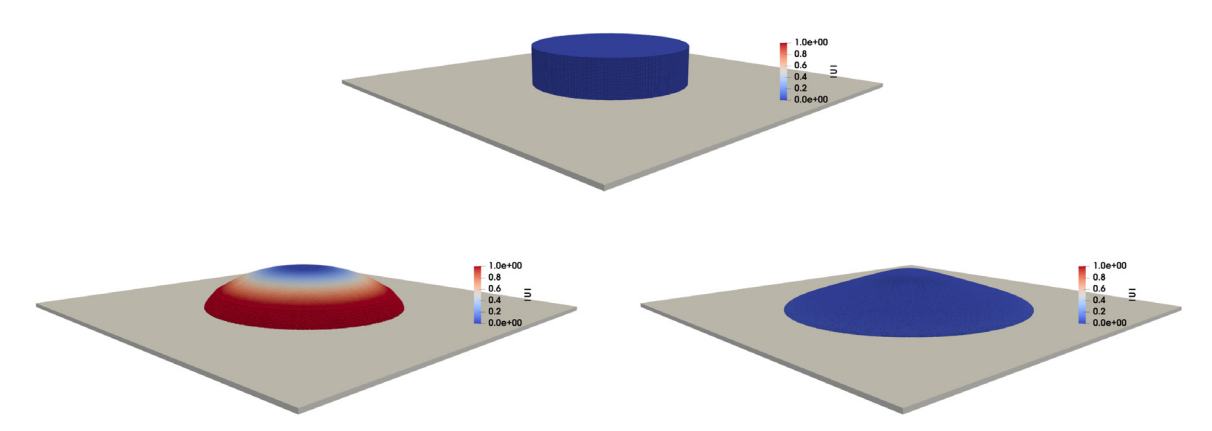


Fig. 4. Angle of repose simulation: Shape of the bulk material at various points during the simulation; color corresponds to the magnitude of velocity (unit: m/s). Radius of the heap in the initial configuration is 0.4 m. Top: initial configuration; left: middle of the settling; right: material is settled.

3. Numerical experiments

The approach proposed is demonstrated in conjunction with five experiments. Three tests, i.e., angle of repose, ball drop, and cone penetration, are used to assess solution accuracy by comparing the results against analytical or experimental data. The last two numerical experiments, plowing and landslide, represent 3D scenarios in which the granular material interacts with solids in a two-way coupling fashion. The plowing involves an L-shaped implement that collides with several stones of nontrivial geometry immersed in the granular material; the landslide is on kilometer scale and involves large prisms that serve as proxies for buildings.

3.1. Angle of repose

The angle of repose experiment is a gravity-driven granular material problem that has been widely treated in the literature in a range of disciplines and application areas, see for instance [85–90]. The granular material is made up of monodisperse spherical particles; the friction coefficient is the same for sphere-to-sphere and sphere-to-plane contact. Under these assumptions, the angle of repose will only be affected by the static friction coefficient μ_s , which for large collections of spheres is related to the angle of repose as $\theta_{repose} = \arctan(\mu_s)$. Continuum-based numerical simulation of this experiment has been reported in the literature. For MPM based simulations, the reader is referred to [91,92]; for SPH studies, see [24,35], where the former discusses a 3D setup, while the latter is a 2D approach used in conjunction with landslides.

Referring to Fig. 4, the heap has an initial height of 0.2 m and radius of 0.4 m; the bulk density of the material is 1500 kg/m³; the static friction coefficient is $\mu_s = 0.3819$ (for both granular material and the floor surface); the granular particle diameter is 0.002 m; the gravitational acceleration is $\mathbf{g} = [0, 0, -9.81]$ m/s². The frictional force between granular material and the floor is captured through several layers of BCE particles fixed on the floor, see for instance Fig. 3. The interaction force between SPH particles and BCE particles was calculated in a similar way that was used to calculate the interaction among SPH particles. The only difference is that the SPH particles' positions will be updated while the BCE particles' positions will not, since the floor was fixed in the simulation. To allow for a larger integration time step, the Young's modulus was relaxed to 2×10^6 Pa. Once released, the granular particles collapse onto the horizontal surface under the gravitational effect and eventually reach a steady state equilibrium. Fig. 4 shows a velocity-field heat map at three points during the simulation: the initial state, mid-way, and in the rest configuration in which the heap assumes a slope at the front tip of 0.3819; i.e., similar to μ_s . In Fig. 5, the same setup was maintained with one exception: the heap radius was changed from 0.2 m to 0.3 m and then 0.4 m. All three setups yielded the same slope at the front tip. In Fig. 6, the heap radius was fixed as 0.2 m but the SPH particle size used to discretize the simulation domain was changed from 0.0025 m to 0.005 m and then 0.01 m. All three setups yielded the same slope at the front tip.

The particle shifting approach introduced in Section 2.4 proved critical in maintaining solution stability and accuracy, thus avoiding the particle disorder at the continuum-boundary interface that has been reported

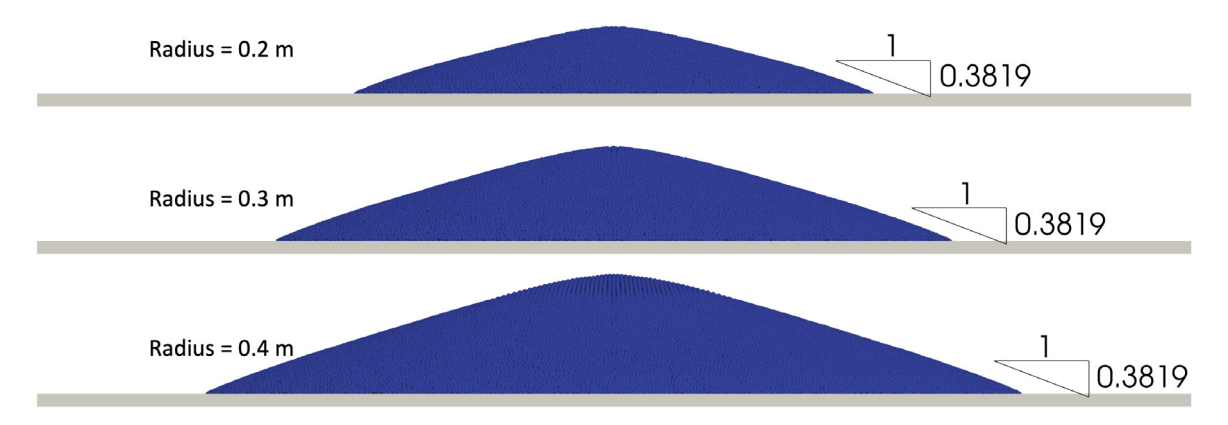


Fig. 5. Side view, angle of repose for different radii of the heap in the initial configuration. The static friction coefficient is $\mu_x = 0.3819$.

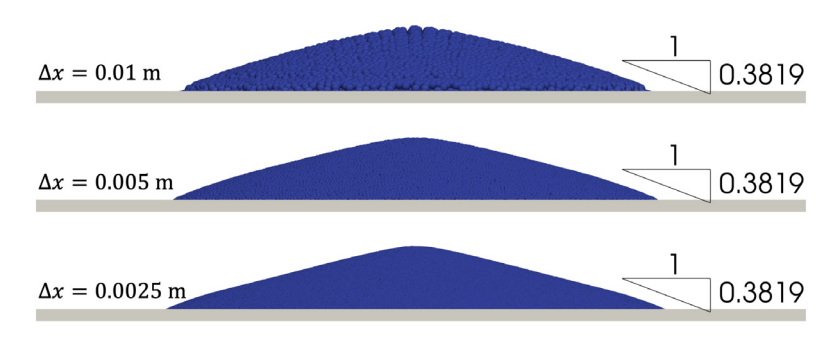


Fig. 6. Side view, angle of repose for different initial spacing. The static friction coefficient is $\mu_s = 0.3819$. Radius of the heap in the initial configuration is 0.2 m.

elsewhere [45–47]. The XSPH term which is expressed in Eq. (13) also contributed to maintaining a stable simulation. To show the difference between simulations with/without using the PPST and XSPH techniques, we set up a group of simulations with four different modes: (a) simulation with both techniques (PPST & XSPH); (b) simulation with only XSPH; (c) simulation with only PPST; (d) simulation with the standard (SD) SPH method. Note that SD is XSPH for $\xi = 0$. Figs. 7 and 8 provide side views and zoom-in views, respectively. The initial radius of the heap was 0.2 m. The two simulations with PPST reach a steady state with good particle distribution; the other two simulations display numerical artifacts. Even though the SD/XSPH results for this test match the analytical solution for the angle of repose, the particle disorder can be detrimental in more complex problems, e.g., the landslide and plowing simulations described herein. For these two problems, without PPST the simulation produced erroneous results or outright did not converge.

It should be pointed out that both PPST and XSPH techniques can influence the momentum balance in the simulations. Numerical tests suggest that their impact is modest. Fig. 9(a) shows the time history of the total kinetic energy of the granular material using different techniques. The simulation with either XSPH or PPST match well the SD results. Assuming the SD results as the "ground truth", we measured the difference between SD results and the other three variants. Fig. 9(b) shows the time history of the relative deviation from the SD kinetic energy (relative to the maximum kinetic energy). The maximum deviation was noted when XSPH and PPST were used in tandem, but the relative deviation was still less than 2%. We also ran simulations with different values of ξ , see Eq. (13), in order to gauge the impact of XSPH alone. Fig. 10 reports the kinetic energy deviation between XSPH and SD. The XSPH technique influences the kinetic energy by 0.8% even when the value of ξ is set as large as 1. For the results reported in this manuscript, all simulations were run with $\xi = 0.5$; this value has led to a stable simulation with marginal change noted in the kinetic energy.

To further validate the influence of the support size, different simulations were run for PPST & XSPH using different kernel lengths. Fig. 11 shows the maximum relative deviation from the SD kinetic energy when the ratio

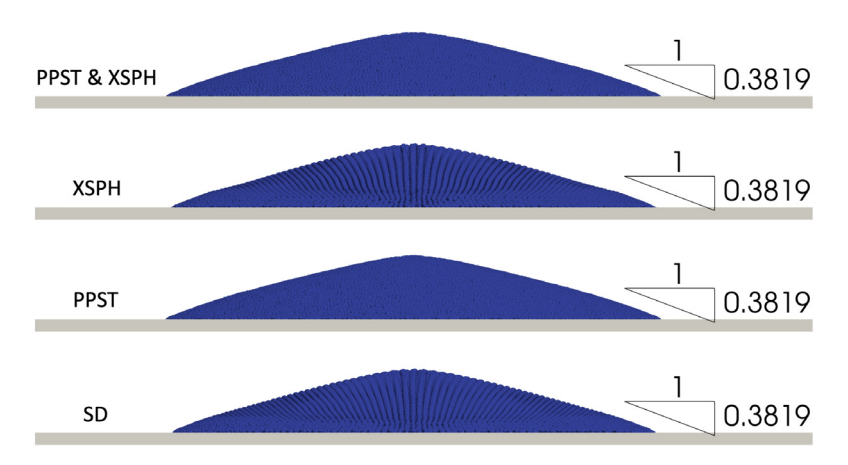


Fig. 7. Side view, angle of repose with different simulation techniques. The static friction coefficient is $\mu_s = 0.3819$. Radius of the heap in the initial configuration is 0.2 m.

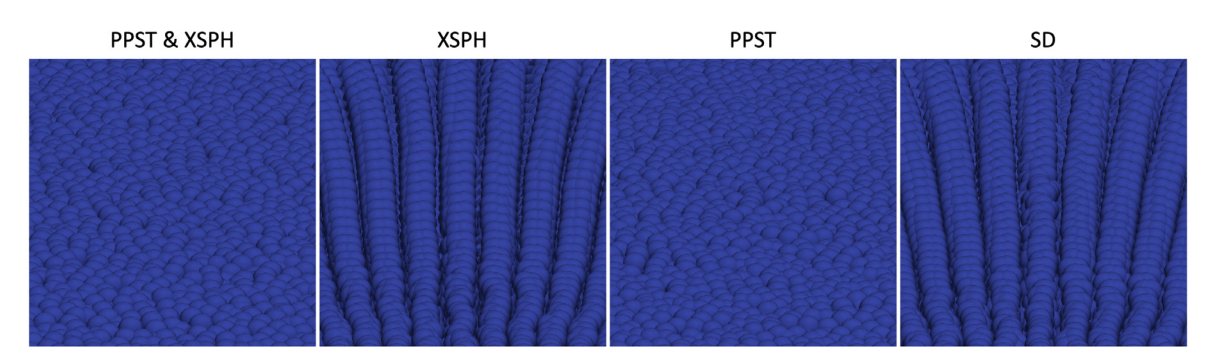


Fig. 8. Local view, angle of repose with different simulation techniques. The static friction coefficient is $\mu_s = 0.3819$.

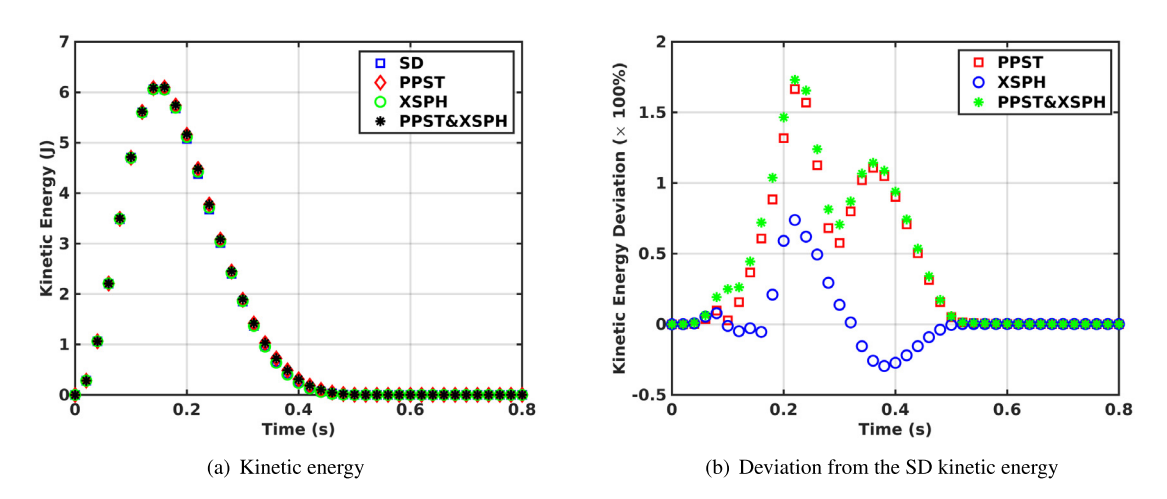


Fig. 9. Time history of the kinetic energy and the deviation from the SD kinetic energy of the granular material with different simulation techniques.

of kernel length and initial particle spacing $(h/\Delta x)$ was changed from 1.0 to 1.6; the ratio $h/\Delta x$ was identically changed in SD and PPST & XSPH. As shown in the figure, the SD vs. PPST & XSPH deviation goes down below 2% and maintains a relatively flat profile. Note that choosing a 1.6 ratio over a 1.0 ratio leads to a four-fold

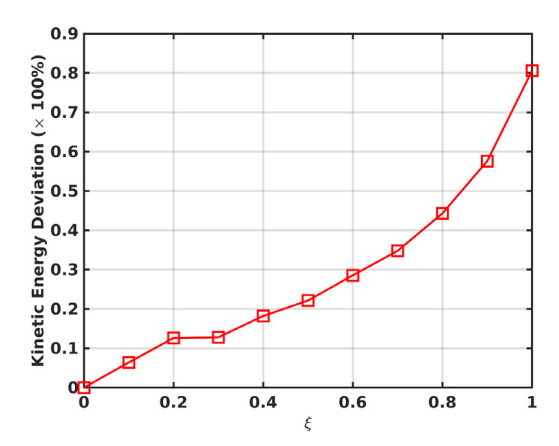


Fig. 10. Deviation from the SD kinetic energy of the granular material for different values of ξ in the XSPH approach.

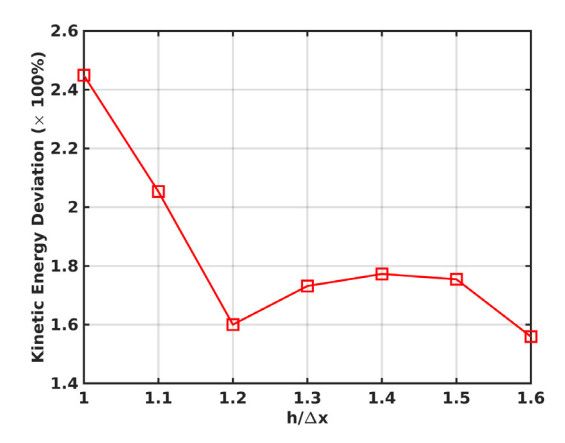


Fig. 11. Deviation from the SD kinetic energy for different sizes of support domain; results reported are for the PPST & XSPH approach.

computational cost increase for a 3D problem. Therefore, to manage simulation run times, the kernel length ratio was set to values between 1.0 and 1.3 for all tests discussed in this contribution.

3.2. Ball drop

This experiment seeks to assess how the continuum model behaves when used to capture the interaction between a large solid and granular material. To that end, a large sphere is dropped from a certain height on a bed of granular material that is represented as a continuum using the approached discussed herein. We use BCE particles attached to the solid body to transmit the "hydrodynamic" force from the "fluid" to the solid body in a two-way coupling mechanism discussed in the previous section.

A similar investigation was previously performed using the DEM method [93], MPM method [94] and physical experiments [95,96]. In all cases, a ball of radius R_{sphere} and density ρ_{sphere} is dropped from a height H_{sphere} above the surface of the granular material, see Fig. 12. The granular material is assumed to have density $\rho_{granular}$ and static friction coefficient μ_s . The static friction coefficient between the ball surface and the granular material is same as that used for the granular material. In this work, we study the low-speed impact of the sphere and compare the results with experimental data reported in [95,96]. For low-speed impact, the penetration depth is roughly the size of the impacting ball. As shown in [95] and later confirmed in [96], the penetration depth D_{sphere} of the ball follows the empirically derived expression

$$D_{sphere} = \frac{0.14}{\mu_s} \left(\frac{\rho_{sphere}}{\rho_{granular}} \right)^{\frac{1}{2}} (2R_{sphere})^{\frac{2}{3}} H_{drop}^{\frac{1}{3}}, \tag{22}$$

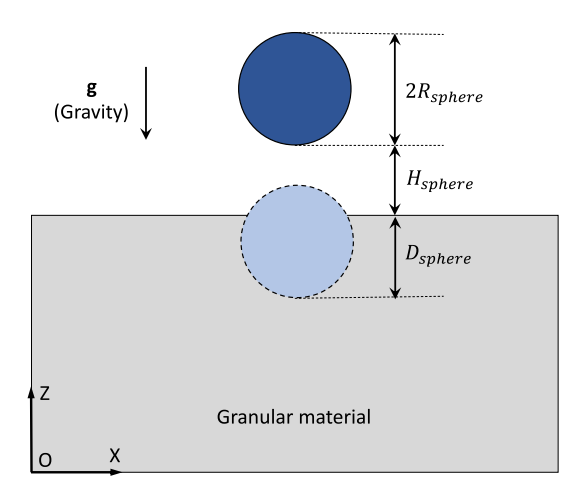


Fig. 12. Schematic of the ball drop experiment, with drop height (H_{sphere}) , sphere radius (R_{sphere}) and the final penetration depth into the granular material (D_{sphere}) .

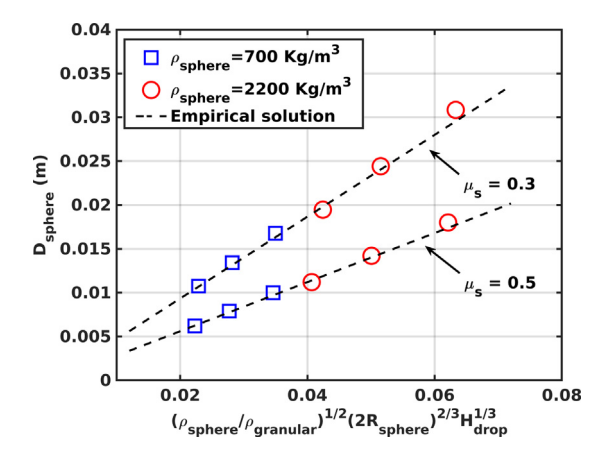


Fig. 13. Penetration depth vs. scaled total drop distance for six simulation experiments run using PPST and XSPH.

where the total drop distance was defined as: $H_{drop} = H_{sphere} + D_{sphere}$. As observed and demonstrated in [96], identical "crater" and penetration depth were observed for different sizes of granular particles, indicating that the particle size does not have a significant effect in the simulation. Thus, we fixed the granular particles' size to 0.001 m in all these simulations. The density of the material was set to 1510 kg/m³. To observe how the static friction coefficient influenced the penetration depth, it was set to 0.3 and 0.5, for two different scenarios. Young's modulus was set to 2×10^6 Pa. In the granular material modeling using the SPH method, Young's modulus only determines how much the material can be compressed. The higher this value, the less the material can be compressed. Note that high Young's modulus values lead to small simulation step sizes Δt . We used a smaller Young's modulus here to be able to use a larger step size. As a rule of thumb, when compression becomes larger than 5% owing to a low Young's modulus value, the SPH solution markedly deviates from the behavior of a granular material.

The radius of the sphere was fixed as 0.0125 m. The drop heights of the sphere were chosen as 0.05 m, 0.1 m and 0.2 m. Two sphere densities were considered: 700 kg/m³ and 2200 kg/m³. Twelve simulations were performed to measure the penetration depth: two choices of static friction coefficient, two choices of sphere densities, three heights from which the sphere was dropped. Fig. 13 shows the penetration depth versus the scaled total drop distance obtained from the twelve simulations. The penetration depth matched well with the linear fitting expression published in [95,96], regardless of the drop height, the sphere density and the static friction coefficient.

Fig. 14 shows the initial setup along with four snapshots from the dynamic simulation; drop height was 0.2 m and density 2200 kg/m³; the static friction coefficient was 0.3. The four snapshots were obtained at t = 0.01 s,

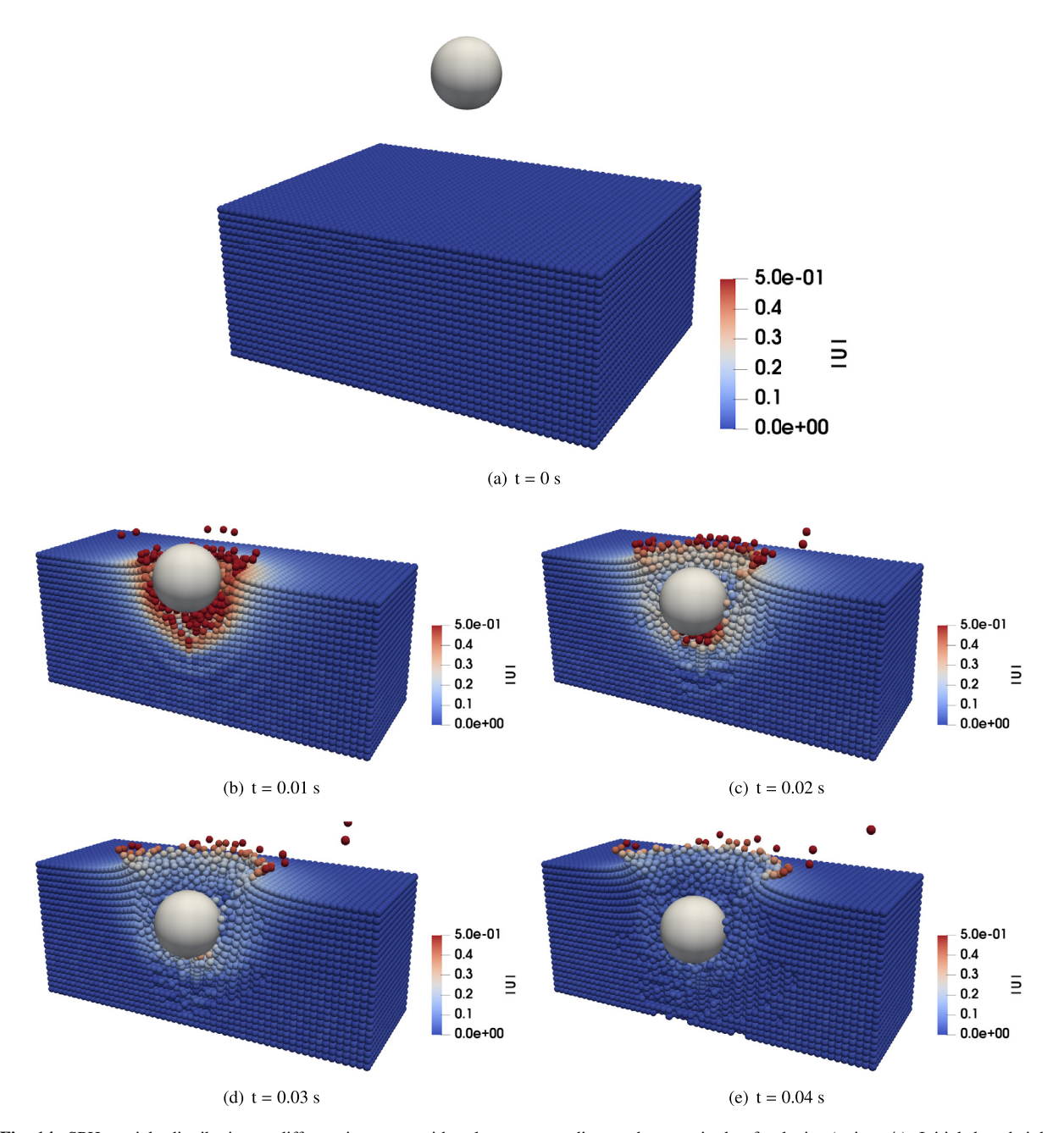


Fig. 14. SPH particle distribution at different instances with color corresponding to the magnitude of velocity (unit: m/s). Initial drop height of the ball is 0.2 m. Both PPST and XSPH enabled. (For interpretation of the references to color in this figure legend, the reader is referred to the web version of this article.)

t = 0.02 s, t = 0.03 s, and t = 0.04 s, respectively. The last snapshot represents the instant of deepest penetration. In all snapshots, each SPH particle is colored according to the magnitude of its velocity; blue represents low velocity, and red represents high velocity. To better demonstrate the "crater", the snapshots show half of the simulation domain through a slice at the center. To investigate how the PPST and XSPH techniques affect the simulation results, we chose the setup that led to the highest red circle shown in Fig. 13, and ran for it a group of simulations with four different solvers that have already been described in the angle of repose problem. Fig. 15 gives the time

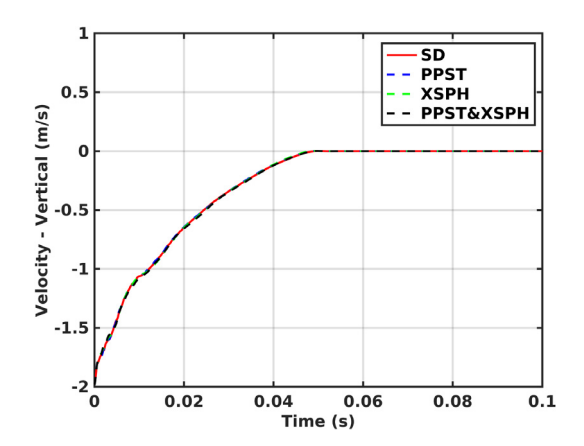


Fig. 15. Time history of the ball's vertical velocity in different simulation modes.

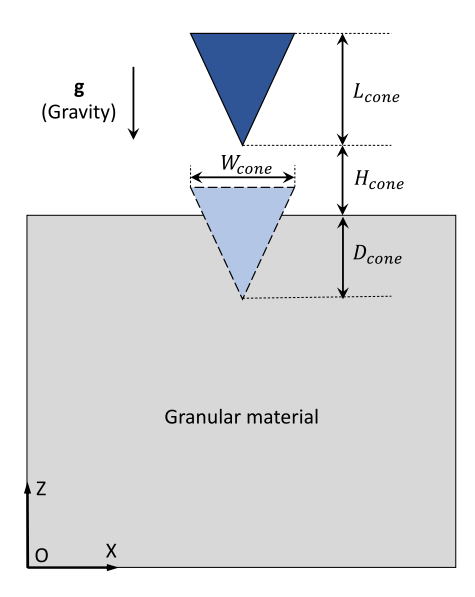


Fig. 16. Schematic of the cone penetration experiment, with drop height (H_{cone}) , cone length (L_{cone}) , cone width (W_{cone}) and the final penetration depth into the granular material (D_{cone}) .

history of the ball's vertical velocity in different simulation modes. All three solvers, with either the XSPH and/or PPST techniques, match well with the standard SPH result. The XSPH technique was employed with $\xi = 0.5$.

3.3. Cone penetration

The goal of this test case was to validate the proposed methodology with nontrivial geometries. The challenge stemmed from the use of the sharp cone tip that cut into the continuum representation of the granular material. This challenged the standard SPH solution, which encountered stability issues. The initial set up of the problem is shown in Fig. 16. The cone's length L_{cone} , width W_{cone} , and mass M_{cone} were set to 0.022 m, 0.02 mm, and 0.1357 kg, respectively. The Young's modulus, density, and Poisson's ratio of the granular material were set to 2×10^6 Pa, 1630 kg/m^3 , and 0.3, respectively. The container filled with granular material had a size of $10 \text{ m} \times 10^6$ Pa, $10 \text{ m} \times 10^6$

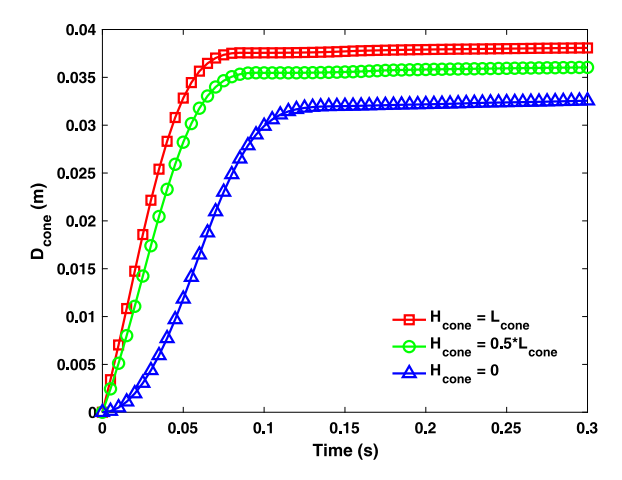


Fig. 17. Penetration depth vs. time for the three drop heights used for the cone with both PPST and XSPH enabled in the simulation. In this validation study, the results match well (max error of approximately 1%) the data published in the literature [11]. (For interpretation of the references to color in this figure legend, the reader is referred to the web version of this article.)

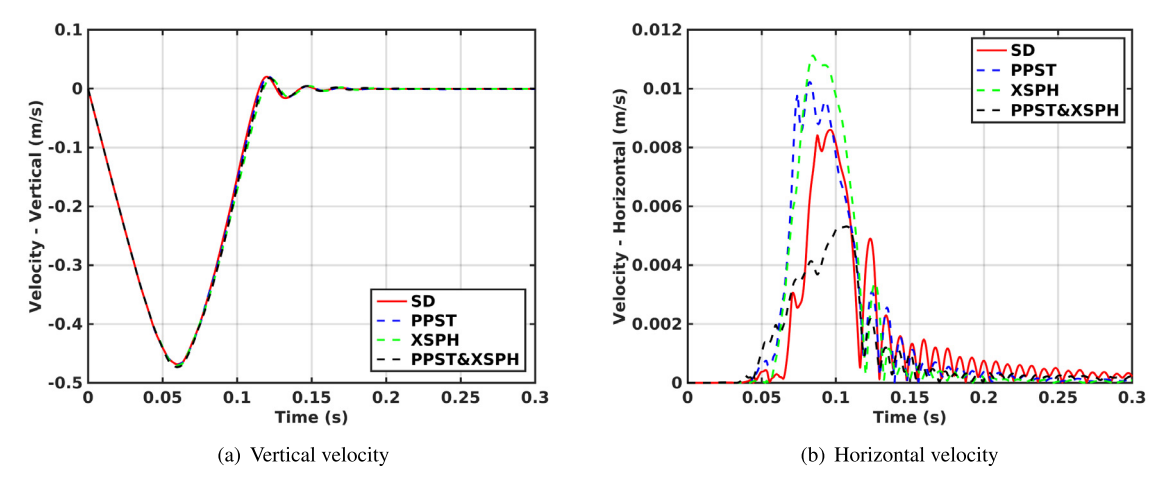


Fig. 18. Time history of the cone's velocity; showing the four methods used to approach the solution: SD, XSPH, PPST, and PPST & XSPH.

was placed right above the granular material surface. The results were compared against data published in [11], which reports both experimental data and results obtained with a fully resolved DEM simulation.

A DEM simulation of this test has two stages. In the first stage, the granular material settles in a process that requires a sizable amount of time [11]. In the second stage, the cone penetrates the material to finally come to rest. In the continuum approach, the first stage is skipped and the cone is placed right above the surface of the granular material with an initial drop velocity of $\sqrt{2gH_{cone}}$. Fig. 17 illustrates the cone penetration depth versus time obtained via the SPH simulation (time t=0 is right at the moment the cone starts penetrating the granular material). The maximum depth increases with the drop height. However, for the tests run, the higher the drop height, the less time it takes to reach steady state. The maximum penetration depths are 3.25 cm, 3.60 cm and 3.81 cm, which matched well (max error of approximately 1%) the data published in the literature [11]: 3.28 cm, 3.56 cm, and 3.85 cm.

This test went through the same regimen: the SD, XSPH, PPST, and PPST & XSPH solutions were tested in conjunction with the lowest dropping height — blue line in Fig. 17. Fig. 18 shows the time history of the cone's velocity in the z direction and in the horizontal plane for the four implementations. The vertical velocities, shown in Fig. 18(a), are very similar; the horizontal component reported in Fig. 18(b) shows larger differences. The XSPH

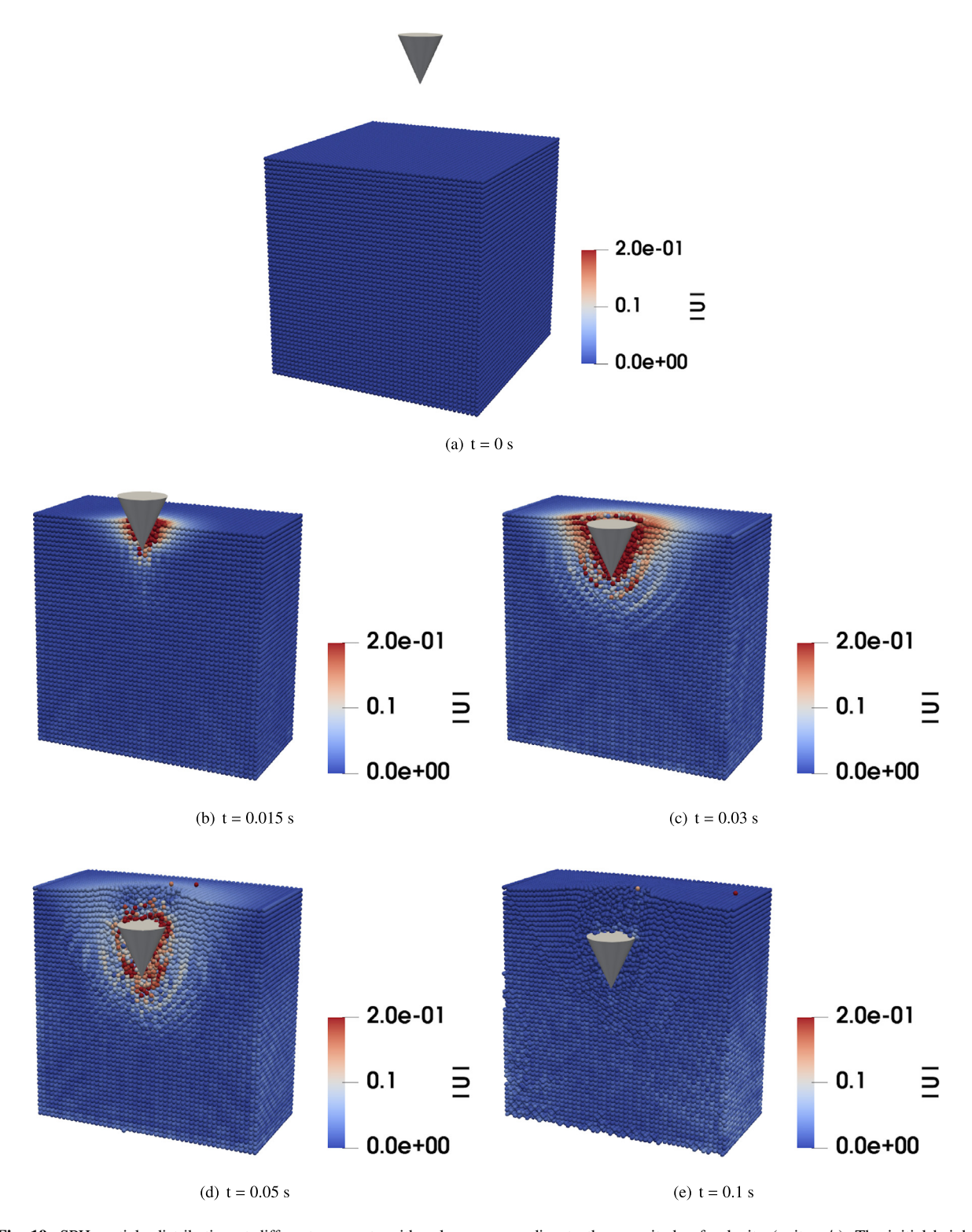


Fig. 19. SPH particle distribution at different moments with color corresponding to the magnitude of velocity (unit: m/s). The initial height of the cone is $H_{cone} = L_{cone}$. Results obtained with PPST and XSPH enabled.

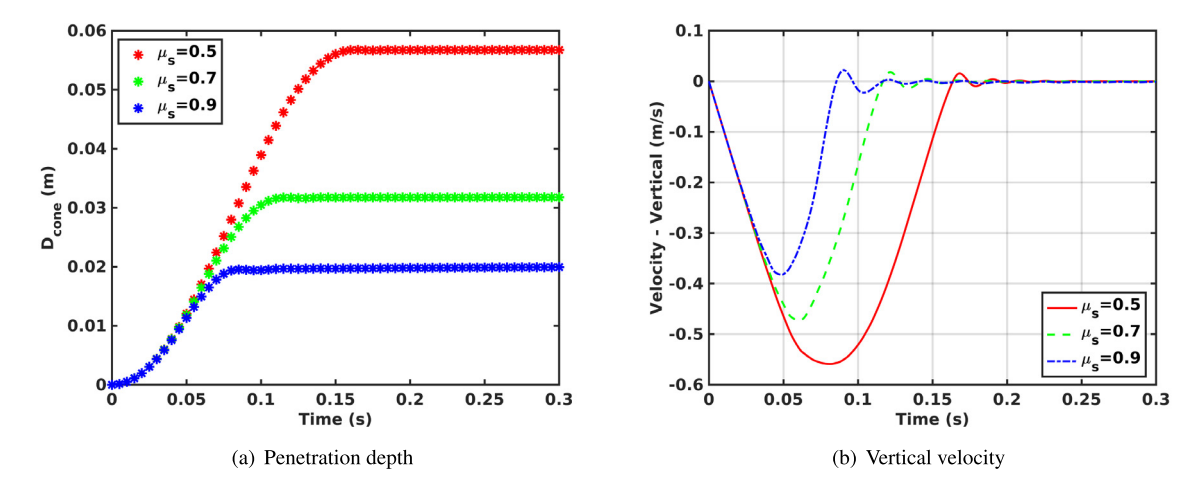


Fig. 20. Penetration depth/vertical velocity vs. time for the three static friction coefficients used for the cone with both PPST and XSPH enabled in the simulation. Zero drop height.

& PPST mode shows the smallest deviation for zero velocity, which would be the expected value owing to the symmetric nature of the test. The XSPH solution used $\xi = 0.5$.

Fig. 19 shows the velocity distributions of the granular material at different time instances for the experiment shown in red line in Fig. 17. The four snapshots were obtained at t = 0.015 s, t = 0.03 s, t = 0.05 s, and t = 0.1 s, respectively. The last snapshot is associated with the deepest penetration. Each SPH particle is colored according to its velocity magnitude, with blue representing low velocity and red representing high velocity.

All cone-penetration results reported thus far were for a friction coefficient 0.7. To investigate the sensitivity with respect to the static friction coefficient, two additional simulations were run in which the static friction coefficient was set as 0.5 and 0.9, respectively. Fig. 20 illustrates the cone penetration depth and vertical velocity versus time obtained using three different static friction coefficient. The results reported are for a zero drop height.

3.4. Landslide and the interaction with the surrounding buildings

The landslide simulation is used to demonstrate the two-way coupling between the dynamics of the granular material and that of several prisms, which are proxies for large buildings. The granular material-like soil was modeled using the SPH particles; the buildings were modeled using rigid bodies that have geometry and can interact with each other and the soil through friction and contact. The scale of this problem, approximately 1.0 km², and a depth of 0.4 km, is in the geomechanics spectrum and thus too large for a fully resolved DEM simulation. The key observation is that the SPH-based computational approach is not sensitive to the size of the SPH particles used to discretize the granular material. As such, as long as the particle size is small relative to the feature length that comes into play (in this case the size of the "buildings"), the methodology outlined is very effective. It should be noted that a problem on this scale stands no chance of being faithfully modeled with the more accurate DEM method since its computational cost would be prohibitively expensive.

The simulation setup is shown in Fig. 21, where a cube of 0.36 km of granular material collapses and in the process hits 27 "buildings". The buildings' height is either 144 m or 96 m. The cross-section of the buildings is $36 \text{ m} \times 36 \text{ m}$. The Young's modulus, density, and Poisson's ratio of the granular material were set to 2×10^8 Pa, 1500 kg/m^3 , and 0.3, respectively. The static friction coefficient of granular material and the building surface was set to $\mu_s = 0.6$. The average diameter of the granular particles used in this simulation was 0.3 m.

Once released, the granular material will hit the buildings, which thereafter move with and in the soil while interacting with each other. After about 50 s, the landslide reaches an equilibrium configuration. Fig. 21 shows the velocity profiles of the granular particles and the position of the buildings at different time instances. The entire dynamics (sped up five times) is available in the supporting information in mp4 format [97]. Noted that since we used relatively larger SPH particles (particle size was 6.0 m) to represent the terrain, we reduced the number of particles by a factor of 8000 of what is required in a DEM simulation, which significantly reduces computational

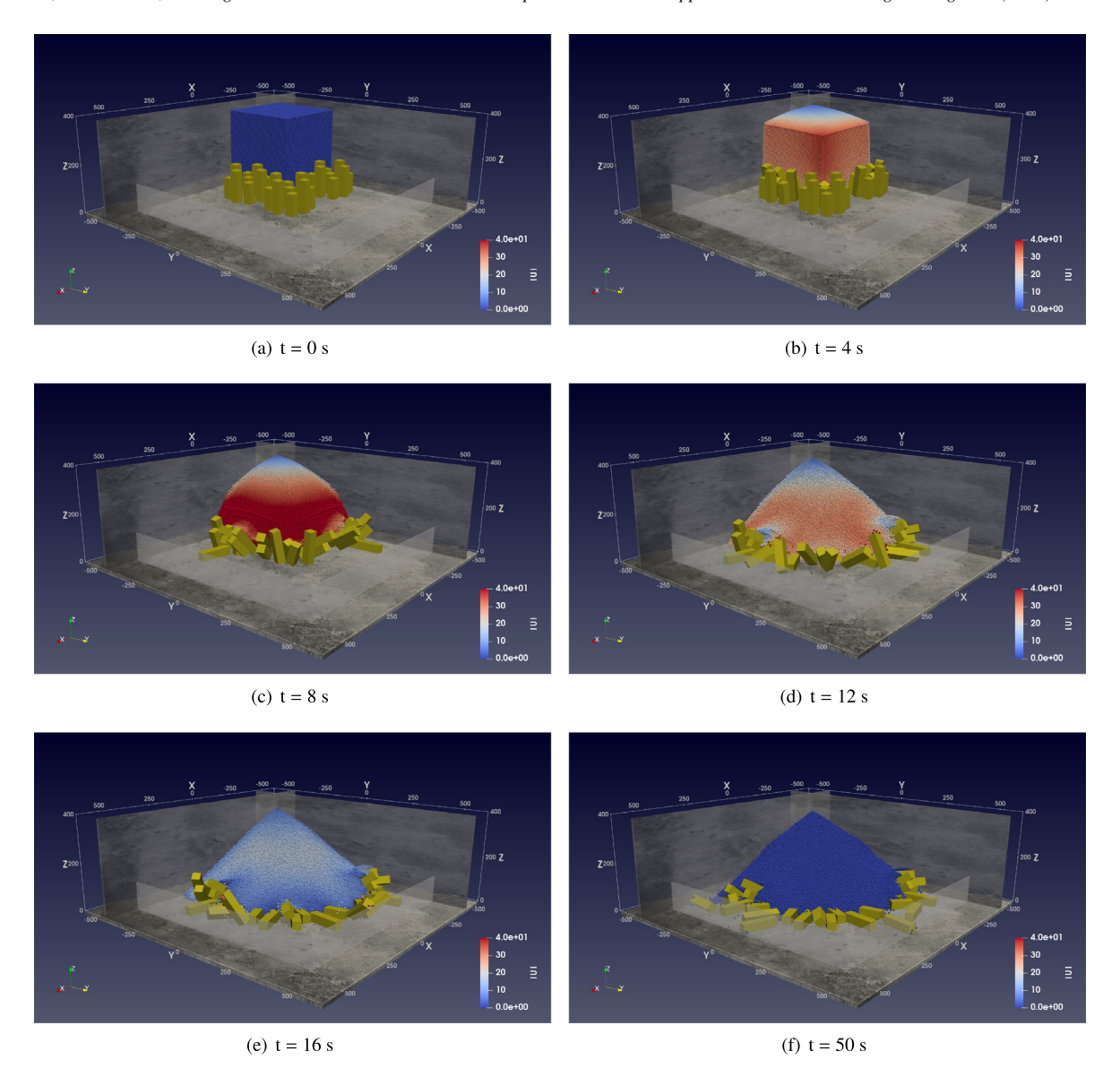


Fig. 21. SPH particle distribution and the 3D motion of the buildings with the color corresponding to the magnitude of particle velocity (unit: m/s). Both PPST and XSPH are enabled.

costs. The total number of SPH particle used to model this problem was $443\,000$; for a $50\,\mathrm{s}$ simulation, the total computational cost was about $5\,\mathrm{h}$ on an Nvidia GTX $1080\,\mathrm{GPU}$ card. The integration stepsize was $5\mathrm{e}{-3}\,\mathrm{s}$.

3.5. Plowing with L-shaped implements

This test is complementary to the landslide discussed in the previous subsection. Therein, the soil moved first and the buildings were engaged in motion. Here, the solid bodies (two plows) move and engage the soil and several other solid bodies (stones). The stones and the plows have nontrivial 3D shapes (see Fig. 22), defined in both cases by triangular meshes. The granular material-like soil was modeled using SPH particles while the plows and stones were modeled as rigid bodies. To handle the interaction between solid bodies (plow, stones) and soil, BCE particles are attached onto the solid bodies using the underlying mesh that defines the rigid body geometry [98]. The solid-to-solid interaction with friction and contact was handled via a penalty approach [99], and called for

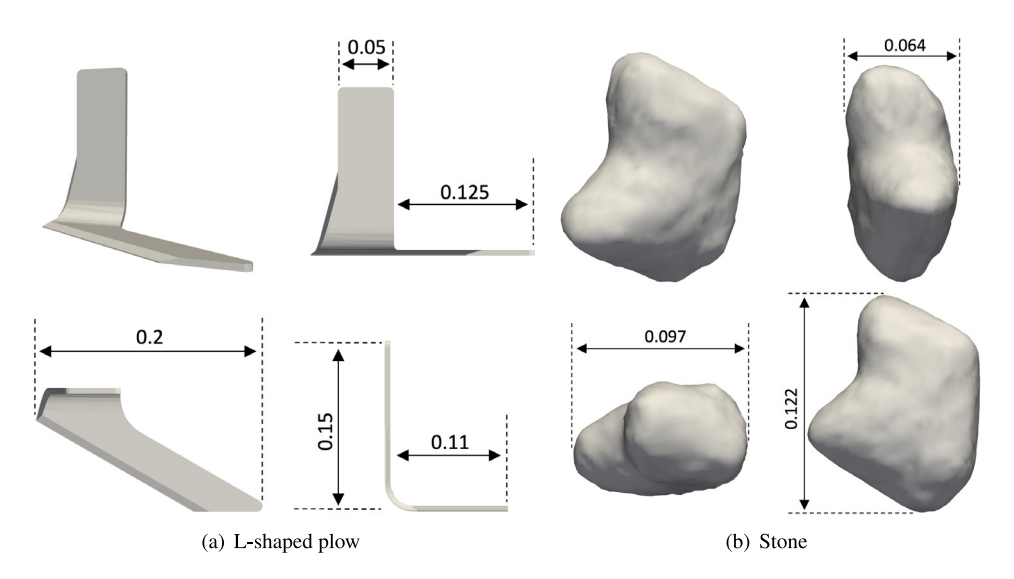


Fig. 22. Sketch of the L-shaped plow and the geometry of the stones used in this simulation (unit: m).

mesh-to-mesh collision detection. For DEM based simulations and experiments, the reader is referred to [100], however, the plow therein has trivial geometry and there is no interaction between the plow and stones. The source code for this test is available in the public domain as open-source, along with a movie of the simulation [97].

The granular material is stored in a container of sizes (L × W × H) 2.0 m × 0.6 m × 0.2 m. The container was filled with granular material-like soil. Ten stones were placed on the soil with random orientations; two L-shaped plows were placed at the right end of the domain. Once started, the plows move with a constant velocity (0.48 m/s) in the soil. The Young's modulus, density, and Poisson's ratio of the granular material were set to 1×10^6 Pa, 1700 kg/m^3 , and 0.3, respectively. The static friction coefficient for the interaction between granular material and the plow/stone surface was set to $\mu_s = 0.25$. Fig. 22 shows the sketch of the L-shaped plow and the geometry of a stone; the obj files are provided in the supporting material. The density of the stone was set as half of the soil's density. The average diameter of the soil particles used in this simulation was 0.001 m while the size of the SPH particles was set as 0.005 m. The total number of SPH particles used to model this problem is 1.96 million. For a 5-second simulation, the total computational cost is about 33 h on one Nvidia GTX 1080 GPU card. The integration stepsize was 2.5e-4 s. Fig. 23 shows the velocity profiles of the granular particles and the position/orientation of the plow/stone at different moments.

This problem was very amenable to a sensitivity analysis test, whose purpose was twofold: gauge the robustness of the solver; and probe its sensitivity and high level predictive attributes relative to changes in the values assumed by three model parameters. In order to avoid the spikes resulting from the collision between the plows and the stones, all stones were removed in these tests. In the first group of simulations, the density of the granular material was set as 1700, 2200, 2700 and 3200 kg/m³, while all other parameters were fixed as before. In the second group of simulations, the static friction coefficient of the granular material was set as 0.15, 0.25, 0.35 and 0.45. In the last group, the depth (distance between the horizontal surface of the plow and the granular material surface) of the plow was set as 0.02, 0.04, 0.06 and 0.08 m. Fig. 24 shows the time history of the drag force exerted on each plow by the granular material for this parametric study. The results come in line with the expectations: (i) The higher the density (also friction coefficient, and depth), the larger the drag force exerted on the plow; (ii) Higher granular material densities damp out the oscillation in the force history; and (iii) High values of the static friction coefficient indicate more oscillatory behavior in the force history. It should be noted that if either the PPST or XSPH techniques are disabled in the simulation, some of the tests with larger friction coefficients or densities become numerically unstable. The snapshots in Fig. 23 were produced with both PPST and XSPH enabled.

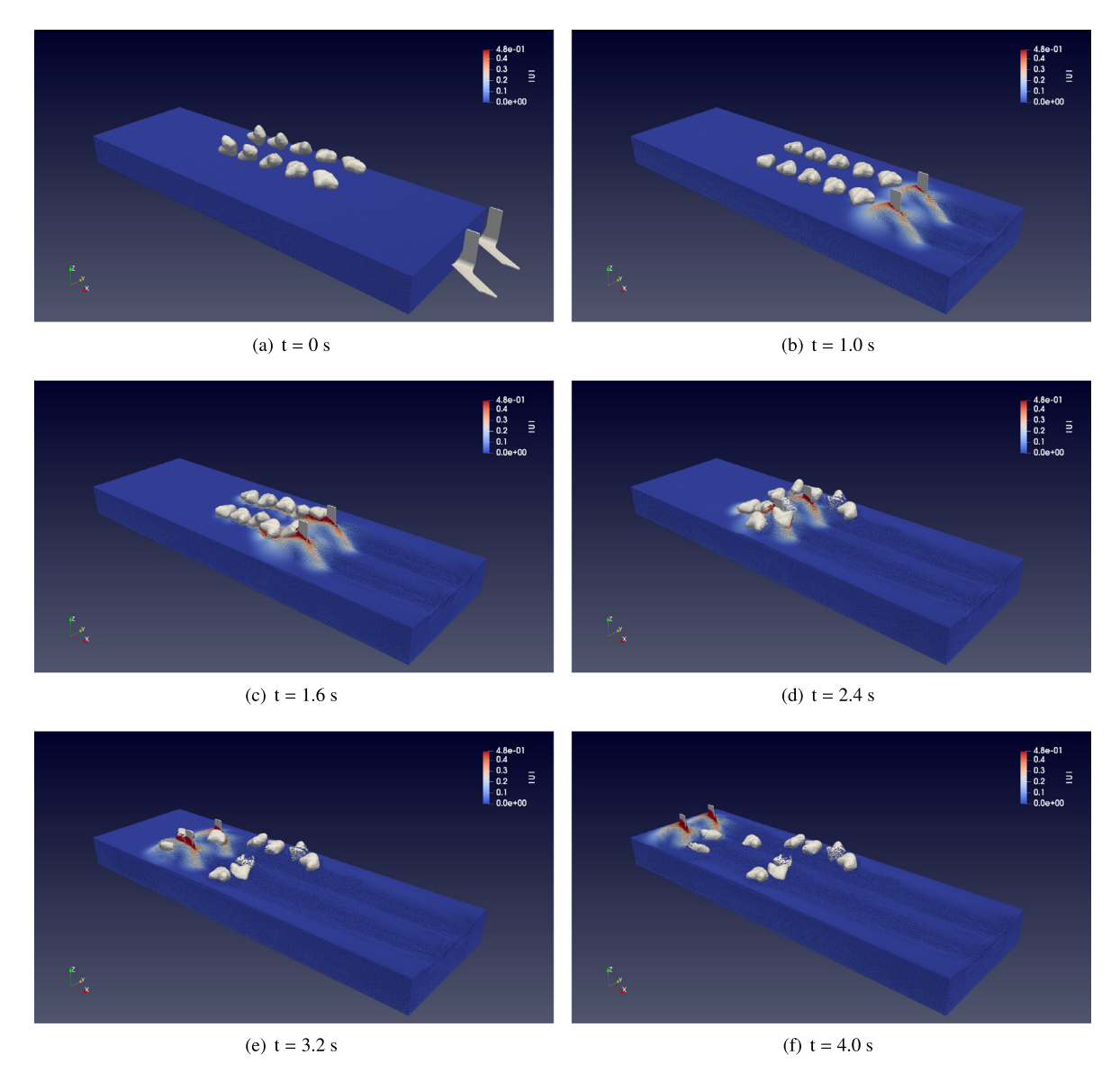
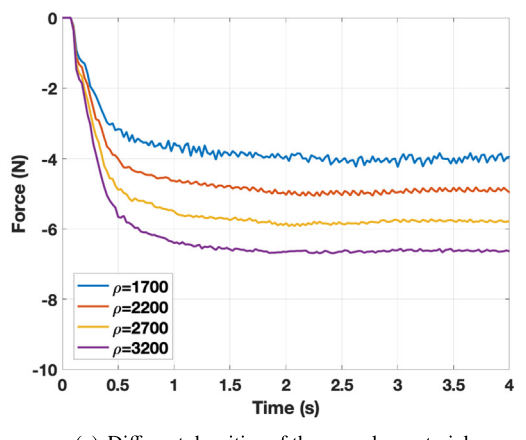
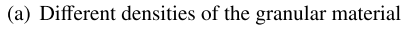


Fig. 23. SPH particle distribution and the 3D motion of the stones with the color corresponding to the magnitude of particle velocity (unit: m/s). Both PPST and XSPH are enabled.

4. Conclusions and directions of future work

This contribution outlines a methodology that employs the SPH method to simulate the dynamics of granular material. The need for a continuum solution is motivated by the observation that in many practical applications, a fully resolved dynamic simulation with DEM is prohibitively long [101]. By comparison, the SPH-based continuum solution discussed reduces both the degree of freedom count and computational cost. The highlight of the methodology discussed is a new penetration-based particle shifting technique (PPST) that anchors the robust treatment of free surfaces. This solution component is critical since in their evolution the SPH particles can lead to scenarios characterized by high particle disorder. The new technique was particularly effective when used in conjunction with the XSPH approach. Compared to solutions that seek to accomplish the same end goal, PPST is easy to implement, robust, accurate, maintains particle regularity over long simulations, and requires





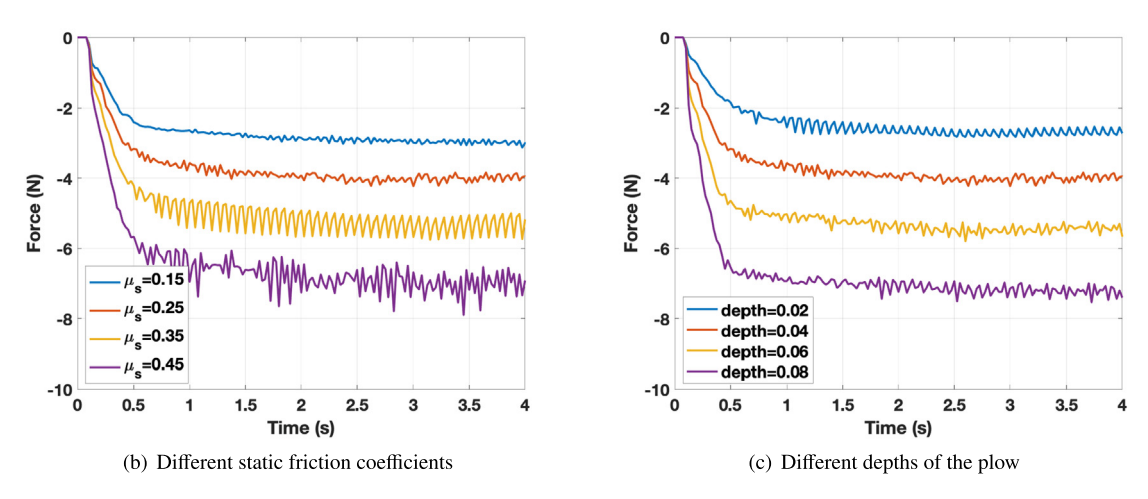


Fig. 24. Time history of the drag force exerted on each plow by the granular material with different value of the parameters. Both PPST and XSPH are enabled.

no extra tracking stage for particles near free surfaces. The key attributes of the methodology outlined and its software implementation are: (i) the approach handles the interaction between granular flows and solid bodies of complex geometries via full, two-way coupling, in a "fluid"–solid interaction style; (ii) the solution captures three-dimensional dynamics; and (iii) the software implementation is open source and available in the public domain for unfettered use [102,103]. To the best of our knowledge, there is no other continuum-based solver for granular dynamics problems whose accuracy/fidelity had been compared against experimental/analytical data and meets (i) through (iii) above.

Looking ahead, there are two aspects that need further attention but fall outside the scope of this contribution: one concerns the implementation of the method; the other has to do with capturing more complex physics. First, with relatively little effort, the speed of the SPH solution can be improved over the preliminary implementation available in the public repository mentioned above. Likewise, the current implementation needs to be improved to support in the same simulation friction coefficients that are different for granular-to-granular interaction, and for granular-to-boundary element interaction; this distinction is not made yet in the code, although the methodology allows it. Second, it is not clear whether the continuum approach and constitutive model employed herein will be a good proxy for granular material of complex morphology, which deviates from the assumption that all particles are spherical and of relatively similar sizes.

Declaration of competing interest

The authors declare that they have no known competing financial interests or personal relationships that could have appeared to influence the work reported in this paper.

Acknowledgments

Support for the first three co-authors was provided by National Science Foundation, US grants CMMI1635004 and CISE1835674. The last two authors were supported by US Army Research Office, under grants W911NF1910431 and W911NF1810476.

References

- [1] A. Ciampalini, F. Bardi, S. Bianchini, W. Frodella, C. Del Ventisette, S. Moretti, N. Casagli, Analysis of building deformation in landslide area using multisensor PSInSARTM technique, Int. J. Appl. Earth Obs. Geoinf. 33 (2014) 166–180.
- [2] L. Antronico, L. Borrelli, R. Coscarelli, G. Gullà, Time evolution of landslide damages to buildings: the case study of Lungro (Calabria, southern Italy), Bull. Eng. Geol. Environ. 74 (1) (2015) 47–59.
- [3] F. Vahedifard, J.D. Robinson, G.L. Mason, I.L. Howard, J.D. Priddy, Mobility algorithm evaluation using a consolidated database developed for wheeled vehicles operating on dry sands, J. Terramech. 63 (2016) 13–22.
- [4] A.M. Recuero, R. Serban, B. Peterson, H. Sugiyama, P. Jayakumar, D. Negrut, A high-fidelity approach for vehicle mobility simulation: Nonlinear finite element tires operating on granular material, J. Terramech. 72 (2017) 39–54, http://dx.doi.org/10.1016/j.jterra.2017. 04.002, URL http://www.sciencedirect.com/science/article/pii/S0022489816301173.
- [5] D. Negrut, H. Mazhar, Sand to mud to fording: Modeling and simulation for off-road ground vehicle mobility analysis, in: International Workshop on Bifurcation and Degradation in Geomaterials, Springer, 2017, pp. 235–247.
- [6] C. Wang, B. Hawlader, D. Perret, K. Soga, Effects of geometry and soil properties on type and retrogression of landslides in sensitive clays, Géotechnique (2020) 1–15.
- [7] J. Fern, A. Rohe, K. Soga, E. Alonso, The Material Point Method for Geotechnical Engineering: A Practical Guide, CRC Press, 2019.
- [8] F. Zhu, J. Zhao, Modeling continuous grain crushing in granular media: a hybrid peridynamics and physics engine approach, Comput. Methods Appl. Mech. Engrg. 348 (2019) 334–355.
- [9] P.A. Cundall, O.D. Strack, A discrete numerical model for granular assemblies, Geotechnique 29 (1) (1979) 47-65.
- [10] M. Furuichi, D. Nishiura, O. Kuwano, A. Bauville, T. Hori, H. Sakaguchi, Arcuate stress state in accretionary prisms from real-scale numerical sandbox experiments, Nat. Sci. Rep. 8 (2018) www.nature.com/scientificreports/.
- [11] A. Pazouki, M. Kwarta, K. Williams, W. Likos, R. Serban, P. Jayakumar, D. Negrut, Compliant contact versus rigid contact: A comparison in the context of granular dynamics, Phys. Rev. E 96 (4) (2017) 042905.
- [12] K. Kamrin, G. Koval, Nonlocal constitutive relation for steady granular flow, Phys. Rev. Lett. 108 (17) (2012) 178301.
- [13] E. Karpman, J. Kövecses, D. Holz, K. Skonieczny, Discrete element modelling for wheel-soil interaction and the analysis of the effect of gravity, J. Terramech. 91 (2020) 139–153.
- [14] G. Mollon, J. Zhao, 3D generation of realistic granular samples based on random fields theory and Fourier shape descriptors, Comput. Methods Appl. Mech. Engrg. 279 (2014) 46–65.
- [15] J. Chauchat, M. Médale, A three-dimensional numerical model for dense granular flows based on the μ (I) rheology, J. Comput. Phys. 256 (2014) 696–712.
- [16] I.R. Ionescu, A. Mangeney, F. Bouchut, O. Roche, Viscoplastic modeling of granular column collapse with pressure-dependent rheology, J. Non-Newton. Fluid Mech. 219 (2015) 1–18.
- [17] N. Guo, J. Zhao, Parallel hierarchical multiscale modelling of hydro-mechanical problems for saturated granular soils, Comput. Methods Appl. Mech. Engrg. 305 (2016) 37–61.
- [18] S. Zhao, J. Zhao, Y. Lai, Multiscale modeling of thermo-mechanical responses of granular materials: A hierarchical continuum–discrete coupling approach, Comput. Methods Appl. Mech. Engrg. 367 (2020) 113100.
- [19] D. Sulsky, Z. Chen, H.L. Schreyer, A particle method for history-dependent materials, Comput. Methods Appl. Mech. Engrg. 118 (1–2) (1994) 179–196.
- [20] S. Bandara, K. Soga, Coupling of soil deformation and pore fluid flow using material point method, Comput. Geotech. 63 (2015) 199–214.
- [21] S. Dunatunga, K. Kamrin, Continuum modelling and simulation of granular flows through their many phases, J. Fluid Mech. 779 (2015) 483–513, http://dx.doi.org/10.1017/jfm.2015.383.
- [22] S. Kularathna, K. Soga, Implicit formulation of material point method for analysis of incompressible materials, Comput. Methods Appl. Mech. Engrg. 313 (2017) 673–686.
- [23] L. Minatti, E. Paris, A SPH model for the simulation of free surface granular flows in a dense regime, Appl. Math. Model. 39 (1) (2015) 363-382.
- [24] C.T. Nguyen, C.T. Nguyen, H.H. Bui, G.D. Nguyen, R. Fukagawa, A new SPH-based approach to simulation of granular flows using viscous damping and stress regularisation, Landslides 14 (1) (2017) 69–81.
- [25] L. Zhan, C. Peng, B. Zhang, W. Wu, Three-dimensional modeling of granular flow impact on rigid and deformable structures, Comput. Geotech. 112 (2019) 257–271.

- [26] A. Pazouki, H. Mazhar, D. Negrut, Parallel collision detection of ellipsoids with applications in large scale multibody dynamics, Math. Comput. Simulation 82 (5) (2012) 879–894.
- [27] G.R. Liu, M.B. Liu, Smoothed Particle Hydrodynamics: A Meshfree Particle Method, World Scientific, 2003.
- [28] Y. Yue, B. Smith, P.Y. Chen, M. Chantharayukhonthorn, K. Kamrin, E. Grinspun, Hybrid grains: adaptive coupling of discrete and continuum simulations of granular media, ACM Trans. Graph. 37 (6) (2018) 1–19.
- [29] K. Soga, E. Alonso, A. Yerro, K. Kumar, S. Bandara, Trends in large-deformation analysis of landslide mass movements with particular emphasis on the material point method, Géotechnique 66 (3) (2016) 248–273.
- [30] A.S. Baumgarten, K. Kamrin, A general fluid-sediment mixture model and constitutive theory validated in many flow regimes, J. Fluid Mech. 861 (2019) 721-764.
- [31] L.B. Lucy, A numerical approach to the testing of the fission hypothesis, Astron. J. 82 (1977) 1013–1024.
- [32] R.A. Gingold, J.J. Monaghan, Smoothed particle hydrodynamics-theory and application to non-spherical stars, Mon. Not. R. Astron. Soc. 181 (1) (1977) 375–389.
- [33] J.J. Monaghan, Smoothed particle hydrodynamics, Rep. Progr. Phys. 68 (1) (2005) 1703–1759.
- [34] H.H. Bui, R. Fukagawa, K. Sako, S. Ohno, Lagrangian meshfree particles method (SPH) for large deformation and failure flows of geomaterial using elastic-plastic soil constitutive model, Int. J. Numer. Anal. Methods Geomech. 32 (12) (2008) 1537–1570.
- [35] W. Chen, T. Qiu, Numerical simulations for large deformation of granular materials using smoothed particle hydrodynamics method, Int. J. Geomech. 12 (2) (2012) 127–135.
- [36] R.C. Hurley, J.E. Andrade, Continuum modeling of rate-dependent granular flows in SPH, Comput. Part. Mech. 4 (1) (2017) 119-130.
- [37] Z. Dai, Y. Huang, H. Cheng, Q. Xu, SPH model for fluid-structure interaction and its application to debris flow impact estimation, Landslides 14 (3) (2017) 917–928.
- [38] X. He, D. Liang, W. Wu, G. Cai, C. Zhao, S. Wang, Study of the interaction between dry granular flows and rigid barriers with an SPH model, Int. J. Numer. Anal. Methods Geomech. 42 (11) (2018) 1217–1234.
- [39] A.M. Abdelrazek, I. Kimura, Y. Shimizu, Simulation of three-dimensional rapid free-surface granular flow past different types of obstructions using the SPH method, J. Glaciol. 62 (232) (2016) 335–347.
- [40] A. Pazouki, D. Negrut, A numerical study of the effect of particle properties on the radial distribution of suspensions in pipe flow, Comput. & Fluids 108 (2015) 1–12.
- [41] M. Rakhsha, A. Pazouki, R. Serban, D. Negrut, Using a half-implicit integration scheme for the SPH-based solution of fluid-solid interaction problems, Comput. Methods Appl. Mech. Engrg. 345 (2019) 100–122.
- [42] W. Hu, Q. Tian, H. Hu, Dynamic simulation of liquid-filled flexible multibody systems via absolute nodal coordinate formulation and SPH method, Nonlinear Dynam. 75 (4) (2014) 653–671.
- [43] A. Pazouki, R. Serban, D. Negrut, A high performance computing approach to the simulation of fluid-solid interaction problems with rigid and flexible components, Arch. Mech. Eng. 61 (2) (2014) 227–251.
- [44] W. Hu, Q. Tian, H. Hu, Simulating coupled dynamics of a rigid-flexible multibody system and compressible fluid, SCIENCE CHINA Phys. Mech. Astron. 61 (4) (2018) 044711.
- [45] R. Xu, P. Stansby, D. Laurence, Accuracy and stability in incompressible SPH (ISPH) based on the projection method and a new approach, J. Comput. Phys. 228 (18) (2009) 6703–6725.
- [46] N. Trask, M. Maxey, K. Kimb, M. Perego, M.L. Parks, K. Yang, J. Xu, A scalable consistent second-order SPH solver for unsteady low Reynolds number flows, Comput. Methods Appl. Mech. Engrg. 289 (2015) 155–178.
- [47] W. Pan, K. Kim, M. Perego, A.M. Tartakovsky, M.L. Parks, Modeling electrokinetic flows by consistent implicit incompressible smoothed particle hydrodynamics, J. Comput. Phys. 334 (2017) 125–144.
- [48] A. Khayyer, H. Gotoh, Y. Shimizu, Comparative study on accuracy and conservation properties of two particle regularization schemes and proposal of an optimized particle shifting scheme in ISPH context, J. Comput. Phys. 332 (2017) 236–256.
- [49] A. Khayyer, H. Gotoh, Y. Shimizu, A projection-based particle method with optimized particle shifting for multiphase flows with large density ratios and discontinuous density fields, Comput. & Fluids 179 (2019) 356–371.
- [50] J.J. Monaghan, SPH without a tensile instability, J. Comput. Phys. 159 (2) (2000) 290-311.
- [51] J.P. Gray, J.J. Monaghan, R. Swift, SPH elastic dynamics, Comput. Methods Appl. Mech. Engrg. 190 (49-50) (2001) 6641-6662.
- [52] Y. Yue, B. Smith, C. Batty, C. Zheng, E. Grinspun, Continuum foam: A material point method for shear-dependent flows, ACM Trans. Graph. 34 (5) (2015) 1–20.
- [53] E.J. Haug, Computer-Aided Kinematics and Dynamics of Mechanical Systems Volume-I, Prentice-Hall, Englewood Cliffs, New Jersey, 1989.
- [54] A. Tasora, M. Anitescu, A convex complementarity approach for simulating large granular flows, J. Comput. Nonlinear Dyn. 5 (3) (2010) 1–10, http://dx.doi.org/10.1115/1.4001371.
- [55] D. Negrut, R. Serban, A. Tasora, Posing multibody dynamics with friction and contact as a differential complementarity problem, ASME J. Comput. Nonlinear Dyn. 13 (1) (2017) 014503, http://dx.doi.org/10.1115/1.4037415.
- [56] D.E. Stewart, Rigid-body dynamics with friction and impact, SIAM Rev. 42 (1) (2000) 3-39.
- [57] D.E. Stewart, J.C. Trinkle, An implicit time-stepping scheme for rigid-body dynamics with inelastic collisions and Coulomb friction, Internat. J. Numer. Methods Engrg. 39 (1996) 2673–2691.
- [58] M. Anitescu, Optimization-based simulation of nonsmooth rigid multibody dynamics, Math. Program. 105 (1) (2006) 113–143, http://dx.doi.org/10.1007/s10107-005-0590-7.
- [59] M. Anitescu, G.D. Hart, A constraint-stabilized time-stepping approach for rigid multibody dynamics with joints, contact and friction, Int. J. Numer. Methods Eng. 60 (14) (2004) 2335–2371.
- [60] D.M. Kaufman, S. Sueda, D.L. James, D.K. Pai, Staggered projections for frictional contact in multibody systems, ACM Trans. Graph. 27 (5) (2008) 164.

- [61] V. Acary, B. Brogliato, Numerical Methods for Nonsmooth Dynamical Systems: Applications in Mechanics and Electronics, Vol. 35, Springer Science & Business Media, 2008.
- [62] F. Bertails-Descoubes, F. Cadoux, G. Daviet, V. Acary, A nonsmooth Newton solver for capturing exact Coulomb friction in fiber assemblies, ACM Trans. Graph. (TOG) 30 (1) (2011) 6.
- [63] D.M. Kaufman, D.K. Pai, Geometric numerical integration of inequality constrained, nonsmooth Hamiltonian systems, SIAM J. Sci. Comput. 34 (5) (2012) A2670–A2703.
- [64] B. Smith, D.M. Kaufman, E. Vouga, R. Tamstorf, E. Grinspun, Reflections on simultaneous impact, ACM Trans. Graph. 31 (4) (2012) 106:1–106:12, http://dx.doi.org/10.1145/2185520.2185602.
- [65] T. Heyn, M. Anitescu, A. Tasora, D. Negrut, Using krylov subspace and spectral methods for solving complementarity problems in many-body contact dynamics simulation, IJNME 95 (7) (2013) 541–561, http://dx.doi.org/10.1002/nme.4513.
- [66] H. Mazhar, T. Heyn, A. Tasora, D. Negrut, Using nesterov's method to accelerate multibody dynamics with friction and contact, ACM Trans. Graph. 34 (3) (2015) 32:1–32:14.
- [67] T. Rabczuk, T. Belytschko, S. Xiao, Stable particle methods based on Lagrangian kernels, Comput. Methods Appl. Mech. Engrg. 193 (12–14) (2004) 1035–1063.
- [68] T. Rabczuk, T. Belytschko, A three-dimensional large deformation meshfree method for arbitrary evolving cracks, Comput. Methods Appl. Mech. Engrg. 196 (29–30) (2007) 2777–2799.
- [69] R. Fatehi, M. Manzari, Error estimation in smoothed particle hydrodynamics and a new scheme for second derivatives, Comput. Math. Appl. 61 (2011) 482–498.
- [70] W. Hu, W. Pan, M. Rakhsha, Q. Tian, H. Hu, D. Negrut, A consistent multi-resolution smoothed particle hydrodynamics method, Comput. Methods Appl. Mech. Engrg. 324 (2017) 278–299.
- [71] W. Hu, G. Guo, X. Hu, D. Negrut, Z. Xu, W. Pan, A consistent spatially adaptive smoothed particle hydrodynamics method for fluid-structure interactions, Comput. Methods Appl. Mech. Eng. 347 (2019) 402–424.
- [72] J.J. Monaghan, On the problem of penetration in particle methods, J. Comput. Phys. 82 (1) (1989) 1–15.
- [73] N.M. Newmark, A method of computation for structural dynamics, J. Eng. Mech. Div. ASCE (1959) 67-94.
- [74] H.M. Hilber, T.J.R. Hughes, R.L. Taylor, Improved numerical dissipation for time integration algorithms in structural dynamics, Earthq. Eng. Struct. Dyn. 5 (1977) 283–292.
- [75] J. Chung, G.M. Hulbert, A time integration algorithm for structural dynamics with improved numerical dissipation: the generalized-α method, Trans. ASME J. Appl. Mech. 60 (2) (1993) 371–375.
- [76] H. Ren, X. Zhuang, T. Rabczuk, H. Zhu, Dual-support smoothed particle hydrodynamics in solid: variational principle and implicit formulation, Eng. Anal. Bound. Elem. 108 (2019) 15–29.
- [77] H. Ren, X. Zhuang, T. Rabczuk, A dual-support smoothed particle hydrodynamics for weakly compressible fluid inspired by the dual-horizon peridynamics, CMES Comput. Model. Eng. Sci. 121 (2) (2019) 353–383.
- [78] H. Takeda, S.M. Miyama, M. Sekiya, Numerical simulation of viscous flow by smoothed particle hydrodynamics, Progr. Theoret. Phys. 92 (5) (1994) 939–960.
- [79] J.P. Morris, P.J. Fox, Y. Zhu, Modeling low Reynolds number incompressible flows using SPH, J. Comput. Phys. 136 (1) (1997) 214–226.
- [80] D.W. Holmes, J.R. Williams, P. Tilke, Smooth particle hydrodynamics simulations of low Reynolds number flows through porous media, Int. J. Numer. Anal. Methods Geomech. 35 (4) (2011) 419–437.
- [81] X. Bian, M. Ellero, A splitting integration scheme for the SPH simulation of concentrated particle suspensions, Comput. Phys. Comm. 185 (1) (2014) 53–62.
- [82] M.S. Shadloo, A. Zainali, M. Yildiz, A. Suleman, A robust weakly compressible SPH method and its comparison with an incompressible SPH, Internat. J. Numer. Methods Engrg. 89 (8) (2012) 939–956.
- [83] J.J. Monaghan, Simulating free surface flows with SPH, J. Comput. Phys. 110 (1994) 399.
- [84] J.J. Monaghan, Smoothed particle hydrodynamics, Annu. Rev. Astron. Astrophys. 30 (1992) 543-574.
- [85] Y. Zhou, B. Wright, R. Yang, B.H. Xu, A.-B. Yu, Rolling friction in the dynamic simulation of sandpile formation, Physica A 269 (2–4) (1999) 536–553.
- [86] Y. Li, Y. Xu, C. Thornton, A comparison of discrete element simulations and experiments for sandpiles composed of spherical particles, Powder Technol. 160 (3) (2005) 219–228.
- [87] D. Markauskas, R. Kačianauskas, Investigation of rice grain flow by multi-sphere particle model with rolling resistance, Granul. Matter 13 (2) (2011) 143–148.
- [88] J. Ai, J.-F. Chen, M. Rotter, J. Ooi, Assessment of rolling resistance models in discrete element simulations, Powder Technol. 206 (3) (2011) 269–282.
- [89] H. Nakashima, Y. Shioji, T. Kobayashi, S. Aoki, H. Shimizu, J. Miyasaka, K. Ohdoi, Determining the angle of repose of sand under low-gravity conditions using discrete element method, J. Terramech. 48 (1) (2011) 17–26.
- [90] S. Geer, M. Bernhardt-Barry, E. Garboczi, J. Whiting, A. Donmez, A more efficient method for calibrating discrete element method parameters for simulations of metallic powder used in additive manufacturing, Granul. Matter 20 (4) (2018) 77.
- [91] E.J. Fern, K. Soga, The role of constitutive models in MPM simulations of granular column collapses, Acta Geotech. 11 (3) (2016) 659–678.
- [92] T. Bhandari, F. Hamad, C. Moormann, K. Sharma, B. Westrich, Numerical modelling of seismic slope failure using MPM, Comput. Geotech. 75 (2016) 126–134.
- [93] T.D. Heyn, On the Modeling, Simulation, and Visualization of Many-Body Dynamics Problems with Friction and Contact (Ph.D. thesis), Citeseer, 2013.

- [94] S. Dunatunga, K. Kamrin, Continuum modeling of projectile impact and penetration in dry granular media, J. Mech. Phys. Solids 100 (2017) 45–60.
- [95] J. Uehara, M. Ambroso, R. Ojha, D.J. Durian, Low-speed impact craters in loose granular media, Phys. Rev. Lett. 90 (19) (2003) 194301
- [96] M. Ambroso, C. Santore, A. Abate, D.J. Durian, Penetration depth for shallow impact cratering, Phys. Rev. E 71 (5) (2005) 051305.
- [97] W. Hu, Continuum modelling of granular material dynamics and its interaction with multibody system using SPH method: Animations, 2020, https://uwmadison.box.com/s/wdffc8ktn24owjhdob98yoqusaejxtrc, Accessed: 2020-11-11.
- [98] F. Gutierrez, C. Ricchio, M. Rakhsha, A. Pazouki, W. Hu, D. Negrut, Investigation of Mesh to Point Cloud Conversion Approaches for Applications in SPH-based Fluid-Solid Interaction Simulations, Tech. Rep. TR-2015-10, Simulation-Based Engineering Laboratory, University of Wisconsin-Madison, 2015, URL https://sbel.wisc.edu/wp-content/uploads/sites/569/2020/05/TR-2015-10.pdf.
- [99] A. Pazouki, M. Kwarta, K. Williams, W. Likos, R. Serban, P. Jayakumar, D. Negrut, Compliant versus rigid contact: A comparison in the context of granular dynamics, Phys. Rev. E 96 (2017) http://dx.doi.org/10.1103/PhysRevE.96.042905.
- [100] E. Kashizadeh, J. Hambleton, S. Stanier, A numerical approach for modelling the ploughing process in sands, in: Computer Methods and Recent Advances in Geomechanics: Proceedings of the 14th International Conference of International Association for Computer Methods and Recent Advances in Geomechanics, 2014 (IACMAG 2014), Taylor & Francis Books Ltd, 2015, pp. 159–164.
- [101] C. Kelly, N. Olsen, D. Negrut, Billion degree of freedom granular dynamics simulation on commodity hardware via heterogeneous data-type representation, Multibody Syst. Dyn. 50 (2020) http://dx.doi.org/10.1007/s11044-020-09749-7.
- [102] Project Chrono Development Team, Chrono: An open source framework for the physics-based simulation of dynamic systems, 2019, https://github.com/projectchrono/chrono, Accessed: 2019-12-07.
- [103] A. Tasora, R. Serban, H. Mazhar, A. Pazouki, D. Melanz, J. Fleischmann, M. Taylor, H. Sugiyama, D. Negrut, Chrono: An open source multi-physics dynamics engine, in: T. Kozubek (Ed.), High Performance Computing in Science and Engineering Lecture Notes in Computer Science, Springer, 2016, pp. 19–49.